Carbon nitride nanotubes anchored with high-density CuN_x sites for efficient degradation of antibiotic contaminants under photo-Fenton process: Performance and mechanism

Xiao Zhang [a], Baokang Xu [a], Shiwen Wang [a], Xi Li [a], Cheng Wang [a], Yanhua Xu [a], Ru Zhou [b], Yang Yu [c], Huaili Zheng [d], Peng Yu [a,*], Yongjun Sun [e,*]

[a] School of Environmental Sciences and Engineering, Nanjing Tech University, Nanjing 211816, China
[b] College of Safety Science and Engineering, Nanjing Tech University, Nanjing 211816, China
[c] Graduate School at Shenzhen, Tsinghua University, Shenzhen 518005, China
[d] Key laboratory of the Three Gorges Reservoir Region's Eco-Environment, State Ministry of Education, Chongqing University, Chongqing 400045, China
[e] College of Urban Construction, Nanjing Tech University, Nanjing 211816, China

ARTICLE INFO

ABSTRACT

The low specific surface area, poor porosity, and weak charge transport caused by the disordered morphology of metal-N-site catalysts are the main factors limiting their environmental applications. Therefore, a hollow-nanotube carbon nitride (Cu-HNCN) catalyst with CuN_x sites dispersed in a hollow nanotube-like CN was constructed and used for the degradation of organic pollutants via the photo-Fenton (PF) process. The high specific surface area, rich porosity, and good visible-light trapping capability of the Cu-HNCN nanotubes were identified. The Cu-HNCN/PF system achieved 96.0% degradation efficiency of tetracycline within 50 min and showed efficient degradation of various antibiotic contaminants. Moreover, the short Cu-N bonds contributed to the improved stability and decreased copper leaching in the Cu-HNCN/PF system. Cu-HNCN, with its enhanced photogenerated charge generation, separation, and transport, was the key to the generation of abundant active species and efficient degradation of pollutants. In addition, frontier electron density theory successfully distinguished the roles of different types of active species in the degradation process. This work provides new insights into the development of catalysts with high stability and accelerated electron transfer to enhance the application of the PF process in practical wastewater purification.

1. Introduction

Antibiotics are commonly used in clinical medicine and animal husbandry and are frequently detected in the environment because they are difficult to biodegrade [1,2]. Antibiotic contaminants and their derivatives can cause the spread of multidrug resistance in the environment, leading to the emergence of drug-resistant genes or bacteria and posing a potential threat to human health and the environment [3,4]. Hence, effective technologies for the treatment of antibiotic contaminants must be developed to reduce environmental risks. Advanced oxidation processes (AOPs) are currently one of the most attractive methods for the treatment of refractory organics, as they activate various peroxides to generate reactive oxygen species (ROS) such as free radicals or singlet oxygen [5,6]. These ROS can effectively mineralize

hard-to-degrade pollutants into carbon dioxide and water.

Fenton oxidation based on hydroxyl radicals (·OH) has been extensively investigated for the removal of refractory pollutants because of its excellent redox potential ($E^0 = 2.73$ V) and strong electrophilic addition property of ·OH [7]. Moreover, the heterogeneous Fenton-like reaction has the advantages of easy catalyst separation, which avoids metal leakage, and environmental compatibility, overcoming the defects of traditional homogeneous Fenton technology [8]. However, the monotonic Fenton-like reaction is limited by H_2O_2 activation efficiency, which limits its applicability in environmental remediation. In general, the medium for the activation of H_2O_2 to form ·OH in Fenton-like reactions is the redox cycle of $M^{n+}/M^{(n+1)+}$ (where M represents the transition metal atoms), and the rate-limiting step is the reduction of $M^{(n+1)+}$ to M^{n+} [9,10]. The heterogeneous visible-light photo-assisted

photo-Fenton (PF) system can enhance the regeneration of subvalent M^{n+} and thus promote H_2O_2 activation through the synergistic effect of green photocatalytic technology and Fenton-like reactions [11,12]. The mechanism of the PF process includes (1) the capture of light energy by the catalyst and photogeneration of electrons, which promote the regeneration of subvalent M^{n+} activators, thus advancing the Fenton-like reaction; (2) effective consumption of photogenerated electrons and release of holes with strong oxidative capability by the optimized electron-hole pair separation, promoting photocatalytic oxidation [13,14]. The PF process can enhance the catalytic rate and mineralization of refractory pollutants owing to its intrinsic synergistic steps.

Copper-based catalysts, which have attracted considerable attention owing to their unique valence electron structures, are widely used as H_2O_2 activators [15,16]. Copper, copper oxides, copper sulfides, and copper-containing polymetallic compounds have been evaluated as catalysts for Fenton-like reactions [17–20]. Catalytic reactions are generally more dependent on isolated atoms than on atoms, emphasizing the utilization of metal atoms [21]. However, the precise synthesis of highly dispersed metal catalysts remains challenging because of the natural diffusion and agglomeration of metal atoms during the synthesis process [22,23]. In addition, catalytic reactions usually occur on the catalyst surface, and unstable metal–carrier interactions can cause metal leaching. Therefore, suitable catalysts with highly dispersed and stable active metal sites must be developed. Graphitic carbon nitride (CN) exhibits the advantages of visible-light response, easy synthesis, non-toxicity, and high stability [24,25]. Its unique "six-fold cavity" with lone electron pair N coordination can provide strong interactions with metal atoms, forming stable metal-N (MN_x) sites, thus achieving highly dispersed metal sites and effectively avoiding leaching due to direct exposure of metals [26,27]. In addition, the heterostructure (Cu-N) can effectively reduce the surface Cu(II) [28,29]. Therefore, CN-based catalysts with CuN_x sites are considered promising for the degradation of refractory pollutants in the PF reaction.

However, primitive CN carriers suffer from defects such as low specific surface area, low porosity, weak charge transport capacity, and insufficient exposure of active centers owing to their disordered two-dimensional (2D) phases [25,30,31]. Notably, nanostructure design, that is, changes in size in certain directions, which lead to changes in quantum confinement, results in highly anisotropic low-dimensional materials with dramatic changes in the electronic structure and physical and chemical properties [32,33]. Hollow nanostructured materials have demonstrated promising applications in heterogeneous catalytic reactions owing to their optimized light trapping and oxidation/reduction species separation [34]. The separation efficiency of photogenerated charges in the hollow nanospheric CN is significantly higher than that in the disordered bulk CN [35]. Moreover, the hollow nanostructure can cause multiple reflections of incident light in the catalyst cavity, thus promoting the utilization of light in the PF reaction. The construction of 1D structural morphology engineering can enlarge the specific surface area of the catalyst and the exposure efficiency of the active sites and provide a pathway for the directional transfer of electrons [36,37], both of which are beneficial for redox reactions that depend on electron transport. Predictably, morphological engineering can achieve high specific surface area, high porosity, efficient light trapping, and fast charge transport of CN carriers [38,39]. Therefore, anchoring Cu species to hollow-nanotube CN (Cu-HNCN) carriers is considered to have the following advantages: (1) enhanced visible-light utilization efficiency, (2) high specific surface area and exposed metal active sites, (3) strong metal–carrier interactions, and (4) excellent charge separation and transport properties. However, the construction of metal-anchored catalysts with 1D and hollow morphologies remains challenging because coatings with highly curved surfaces are difficult to control [40]. However, once prepared, such catalysts may become outstanding environmentally functional materials with practical application potential.

In this study, Cu-HNCN catalysts with highly dispersed CuN_x sites were prepared and used as PF catalysts for the degradation of antibiotic contaminants. Tetracycline (TET), which is widely used and released into the environment as an animal growth promoter to enhance growth rate and feed conversion, was selected as a model contaminant [41]. Characterization determined the morphological structure and form of active sites present in the Cu-HNCN catalyst. The effects of H_2O_2 concentration, catalyst dosage, pH, TET concentration, coexisting substances, and the real water matrix on TET degradation during the PF process were investigated. Density functional theory (DFT) calculations clarified the configuration of Cu-HNCN and the role of the morphological structure in charge transport. Various active substances and their roles in the reaction were identified and a catalytic degradation mechanism was proposed. Finally, the TET degradation pathway was proposed based on frontier electron density (FED) calculations and liquid chromatography-mass spectrometry (LC-MS).

2. Materials and methods

2.1. Materials

The source and type of materials used are provided in Supporting Material Text S1.

2.2. Synthesis of catalysts

HNCN was prepared according to a modified method reported by Xu et al. [35]. First, 2 g melamine and 2 g cyanuric acid were dissolved in 40 ml deionized water, mixed, and stirred at room temperature for 10 min. Then, the mixed solution was placed in a 150 ml autoclave with a polytetrafluoroethylene lining and kept at 200 °C for 12 h under magnetic stirring. The obtained intermediate was dried under vacuum at 60 °C. Finally, the product was fully ground, placed in a covered ceramic crucible, heated to 550 °C at 5 °C/min under nitrogen, and maintained for 4 h. The final product was obtained by natural cooling.

The Cu-HNCN catalyst was prepared by a similar procedure. A total of 0.303 g Cu(NO$_3$)$_2$.3 H$_2$O was weighed, dissolved in 10 ml deionized water, and sonicated for 10 min. The copper source solution was then added dropwise to a mixture of 2 g melamine and 2 g cyanuric acid. The subsequent steps were the same as those used for preparing HNCN. The final product was denoted as 2Cu-HNCN (where 2 represents the mass percentage of Cu/melamine + cyanuric acid).

Disordered CN and Cu-anchored CN (Cu-CN) were prepared using a similar method without hydrothermal treatment, and the mixed solution was stirred at 100 °C until the moisture was completely removed and then calcined following the same procedure.

2.3. Characterizations

The characterization instruments and parameters used for the catalyst characterization are provided in Supporting Material Text S2.

2.4. Catalytic performance evaluation

All degradation processes were carried out in a 150 ml quartz reactor, which was equipped with circulating water to maintain the reaction temperature at 20 ℃. The TET concentration was 10 mg/L. After the catalyst was added, the reaction gel was pre-stirred for 30 min in the dark to reach the adsorption–desorption equilibrium. Then, H_2O_2 was added, and the light source was turned on to initiate the degradation process. The light source was a 300 W xenon lamp (CEL-HXF300, CEAULIGHT, China) equipped with a filter ($>$420 nm), and the light density was maintained at 100 mW/cm^2. At a preset time, a 3 ml sample was obtained and passed through a 0.22 μm filter membrane. The initial pH was adjusted using 0.1 M HCl or 0.1 M NaOH. The catalytic reaction kinetics were obtained using a fitted first-order reaction kinetics

equation. In Eq. (1), C_0 represents the initial concentration of the pollutants, C_t denotes the real-time concentration of the pollutants, and k_{obs} is the rate constant of the fitted first-order kinetics. The catalyst was then collected via centrifugation.

$$-\ln\left(\frac{C_t}{C_0}\right) = k_{obs} \tag{1}$$

2.5. Analytical methods

All information on the equipment model and experimental methods is provided in Supporting Material Text S3.

2.6. Theoretical computation

The details of the theoretical computation are provided in Supporting Material Text S4.

3. Results and discussion

### 3.1. Characterization

3.1.1. Morphology and structural analysis

As shown in Scheme 1, the Cu-HNCN catalyst was prepared using Cu(NO$_3$)$_2$.3 H$_2$O, melamine, and cyanuric acid as the raw materials. Fig. 1a and b show the apparent morphology of the precursor after hydrothermal treatment. The precursor sample exhibited a regular cavity composed of multiple reduced 2D planes with a cavity diameter of approximately 5.8 μm. Notably, the morphology of the sample changed significantly after calcination. As shown in Fig. 1c and d, the 2D planes of HNCN collapsed significantly and generated regular nanotubes with mesopores of approximately 2.7 μm in length and 70–90 nm in diameter. Moreover, the transmission electron microscopy (TEM) image of HNCN showed preserved nanotubes after 2D planar collapse (Fig. 1e), whereas the diameter of the nanotubes was close to that observed in the scanning electron microscopy (SEM) image and exhibited a porous shape (Fig. 1f). Fig. 1g shows that HNCN exhibited single-layered tube walls, indicating a hollow interior that can facilitate the increase in specific surface area and the exposure of internal active sites [42]. Fig. 1h and i show the SEM images of the Cu-HNCN catalysts. The Cu-HNCN catalysts exhibited severe collapse after thermal polymerization and retained regular pore-rich nanotubes with diameters in the range of 70–80 nm. Additionally, the Cu, C, and N species were uniformly distributed on the surface of the Cu-HNCN catalyst (Fig. 1j). Furthermore, TEM images of the Cu-HNCN catalyst confirmed that the catalyst had a monolayer porous tube wall (Fig. 1k and l) with a mesopore size of approximately 20–30 nm. No copper-containing nanoparticles were found on the surface of Cu-HNCN, and no lattice fringes attributable to copper oxides or copper-carbon clusters were observed in the high-resolution TEM image (Fig. 1m), indicating that neither copper oxides nor copper-carbon clusters were present in Cu-HNCN. The hollow porous properties of the nanotubes in the catalyst were further demonstrated by high-angle annular dark-field (HAADF) imaging (Fig. 1n). The HAADF-mapping images showed a high distribution and size uniformity of Cu, C, and N atoms on the Cu-HNCN surface. Meanwhile, the Cu and N atoms were distributed with uniform adjacency, suggesting the possible presence of Cu-N complexation sites [43]. By contrast, the Cu and O atoms were distributed with large spacing, which in turn proved the absence of Cu-containing oxides. The SEM and TEM images suggest that the Cu species were highly dispersed on HNCN. In addition, Cu-CN was present in the disordered 2D sheets, and the Cu species were highly dispersed (Fig. S1).

Fig. S2a shows the N$_2$ adsorption–desorption curves of different catalysts. All samples showed an H4 hysteresis loop, indicating that abundant pores were present in the CN matrix [44]. The pore size distribution curves (Fig. S2b) showed that the HNCN and Cu-HNCN catalysts possessed large average pore sizes and pore volumes, which can be attributed to their rich pore structures. Table 1 summarizes the structural characteristics of CN, Cu-CN, HNCN, and Cu-HNCN. The Brunauer–Emmett–Teller (BET) specific surface area of HNCN reached 80.59 m^2/g, which is larger than that of disordered CN (59.20 m^2/g). In addition, the pore volume and size of HNCN were significantly larger than those of CN (0.594 cm^3/g and 29.60 nm vs. 0.263 cm^3/g and 18.05 nm). Therefore, the large specific surface area of HNCN is consistent with its rich pore structure. Although the specific surface area, pore volume, and pore size of Cu-HNCN were slightly reduced (73.87 m^2/g, 0.498 cm^3/g, and 26.98 nm) because of the anchoring of Cu (the pore diameter was consistent with the results observed in the TEM image), they were significantly larger than those of Cu-CN (54.41 m^2/g, 0.255 cm^3/g, and 17.85 nm). These results revealed the good mesoporous properties of the Cu-HNCN catalyst, which are conducive to the exposure of active sites in the redox reaction [45]. The thermogravimetric curves of the Cu-CN and Cu-HNCN catalysts showed that their Cu contents were approximately 10.59% (Cu-CN) and 11.53% (Cu-HNCN) (Fig. S3). Inductively coupled plasma spectrometry (MS) was used to further determine the Cu content in the catalysts (Table S1).
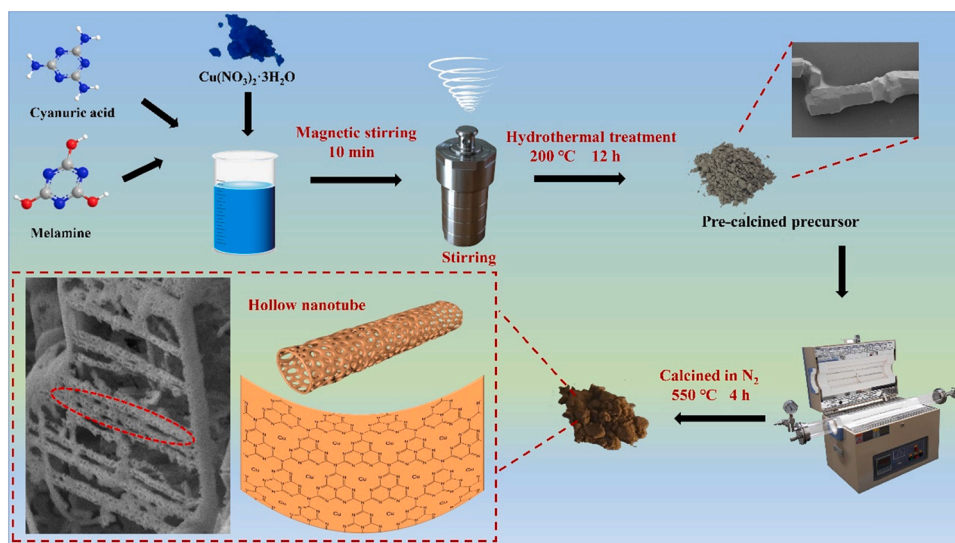
Scheme 1. Preparation of Cu-HNCN catalyst.
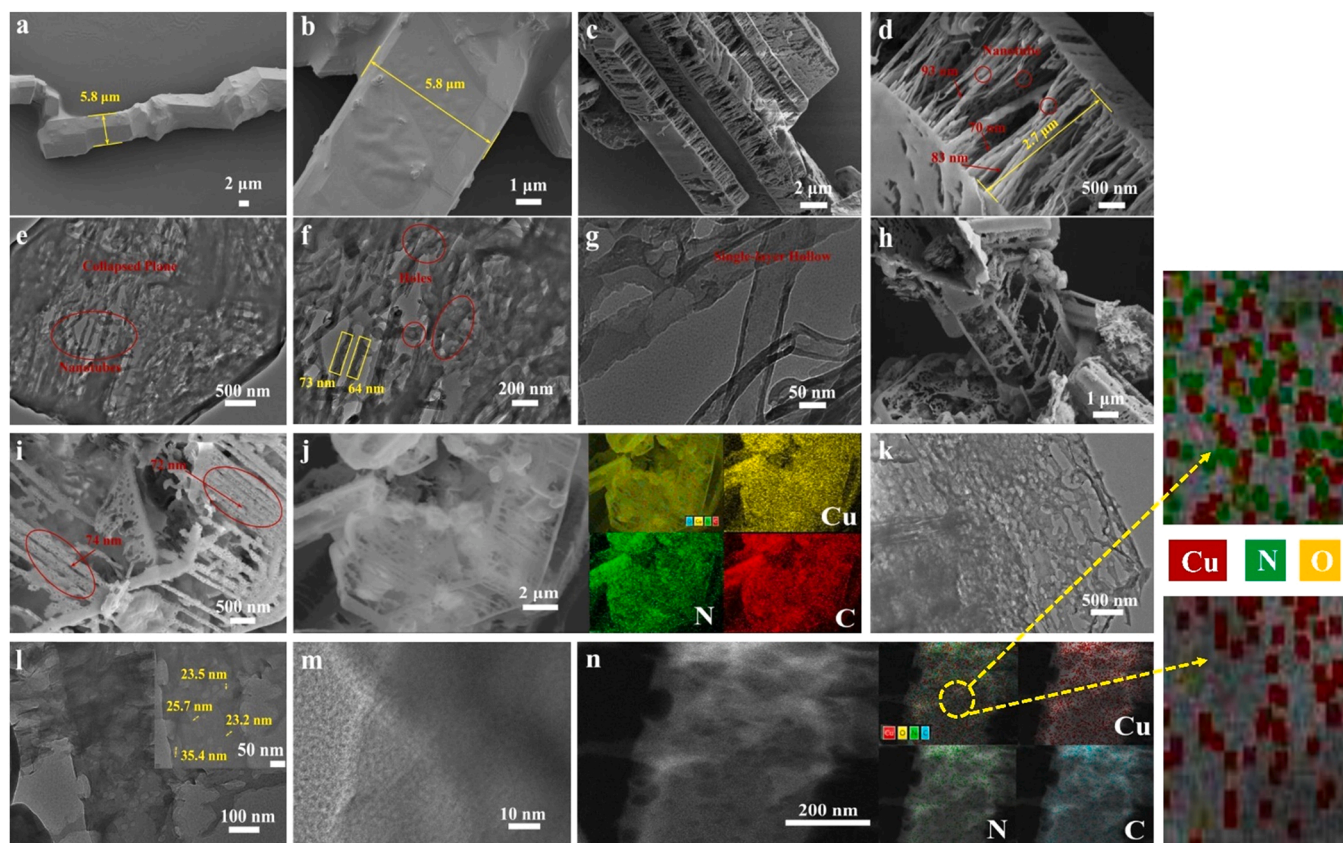
Fig. 1. SEM images of precursor: (a) 2 and (b) 1 μm. SEM images of HNCN catalyst: (c) 2 μm; (d) 500 nm. TEM images of HNCN catalyst: (e) 500, (f) 200, and (g) 50 nm. SEM images of Cu-HNCN catalyst: (h) 1 μm and (i) 500 nm. Elemental mapping images: (j) 2 μm. TEM images of Cu-HNCN catalyst: (k) 500, (l) 100, and 50 and (m) 10 nm. HAADF-scanning TEM and elemental mapping images: (n) 200 nm.

Table 1
Specific surface area, pore volume, and pore diameter of different catalysts.

| Catalysts	S_{BET} (m^2/g)	Total pore volume (cm^3/g)	Pore diameter (nm)
CN	59.20	0.263	18.05
Cu-CN	54.41	0.255	17.85
HNCN	80.59	0.594	29.60
Cu-HNCN	73.87	0.498	26.98

The accurate Cu contents were 9.68 and 10.72 wt% for Cu-CN and Cu-HNCN, respectively.

The phase structure of the catalysts was determined using X-ray diffraction (XRD). As shown in Fig. 2a, the characteristic diffraction of the CN and HNCN samples at 27.3° was attributed to the interlayer stacked (002) crystalline phase of CN. The intensity of the (002) peak of HNCN was weak, which may be attributed to the size-dependence of the nanotubes [46]. In addition, the (002) characteristic diffraction of Cu-CN and Cu-HNCN slightly shifted to higher angles, and the conjugate plane spacing was reduced to 0.321 and 0.319 nm compared with the 0.329 and 0.323 nm, respectively, compared to those of CN and HNCN. Evidently, Cu doping affected the growth of CN crystals. Moreover, the intensity of the peak attributed to the (100) crystal plane at 13.2° was weaker in HNCN than in CN and almost invisible in Cu-HNCN, indicating that the nanotubes had a small planar layer size [47]. The anchor of Cu did not destroy the CN matrix phase, and no copper oxides or copper–carbon cluster diffraction peaks appeared in Cu-HNCN, indicating that none of the Cu species existed as copper oxides or copper–carbon clusters. Fourier infrared (FTIR) spectroscopy was performed to study the local chemical characteristics of the catalysts. As shown in Fig. 2b, the IR bands of Cu-CN, HNCN, and Cu-HNCN were

consistent with those of the original CN, indicating the stability of the CN matrix. However, the intensities of Cu-CN and Cu-HNCN were slightly weaker than those of CN and HNCN in the 1228 and 1314 cm^{-1} bands, corresponding to N-(C$_3$) and C═N-C vibrations, respectively, in aromatic heterocyclic compounds. This phenomenon was attributed to the coordination of the N point in CN with the Cu atom, which affected the stretching vibration of the aromatic heterocyclic ring [16,29]. Moreover, significantly enhanced absorption vibrations of HNCN and Cu-HNCN in the 3000–3500 cm^{-1} band, which correspond to surface-bonded water molecules and amino groups, were observed, indicating that HNCN and Cu-HNCN have large open surfaces [48] because of the successful construction of hollow nanotubes.

The elemental composition and electronic properties of Cu-HNCN were investigated by X-ray photoelectron spectroscopy (XPS). Table S2 lists the atomic compositions of all samples. As shown in Fig. 2c, the peaks at 284.5, 286.6, and 287.9 eV in the C 1 s spectrum of CN are attributed to sp^2 C and C-NH$_x$ (x = 1, 2) at the edge of the heptazine unit and N-C═N [49]. The construction of HNCN and the anchoring of Cu caused no change in the C 1 s spectrum. Several changes were observed in the N 1 s spectrum (Fig. 2d). The peaks at 398.5, 399.6, and 400.9 eV in CN were attributed to N (N-C═N), N-(C$_3$), and NH$_x$ (x = 1, 2), respectively [50]. By contrast, the peaks of N (N-C═N) and N-(C$_3$) in HNCN shifted slightly to lower binding energies, and the area of the NH$_x$ (x = 1, 2) peaks was reduced. This phenomenon was attributed to the changes in bond energy between C and N atoms caused by the plane bending of HNCN [51], whereas the reduction in plane edges containing NH$_x$ (x = 1, 2) was attributed to the construction of nanotubes. Cu-HNCN exhibits a peak at 399.3 eV, which is attributed to the coordinated nitrogen in CuN$_x$ [52]. In addition, the peaks of N (N-C═N), N-(C$_3$), and NH$_x$ (x = 1, 2) shifted to higher binding energies than those of HNCN, indicating that the appearance of Cu atoms reduced the
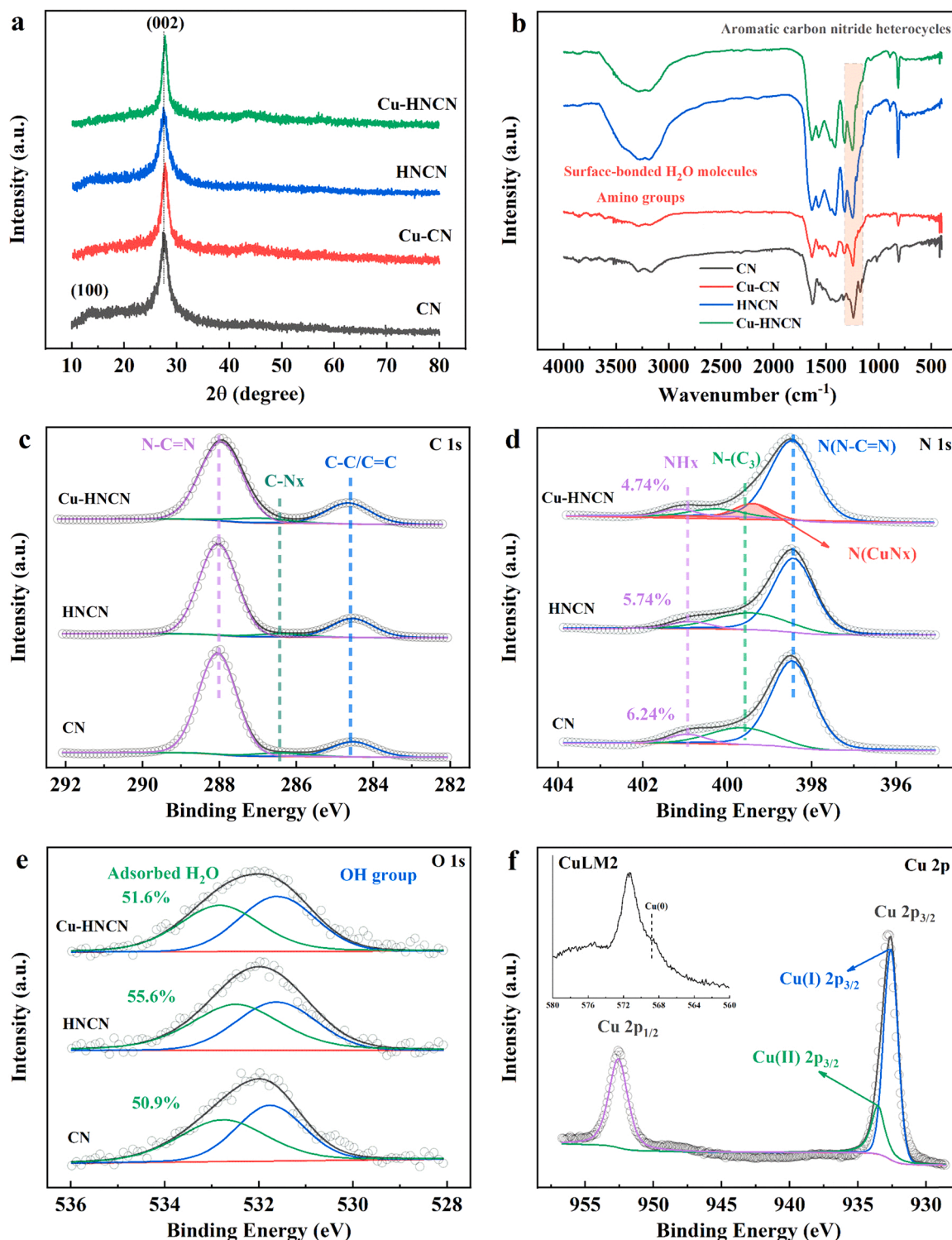
Fig. 2. (a) XRD patterns and (b) FTIR spectroscopy spectra of CN, Cu-CN, HNCN, and Cu-HNCN. XPS of (c) C 1s, (d) N 1s, and (e) O 1s spectra of CN, HNCN, and Cu-HNCN. (f) Cu 2p spectrum and Cu LM2 Auger spectrum (inset) of Cu-HNCN.

electron density of N atoms, resulting from the formation of Cu-N co-ordination bonds [16]. Notably, the surface content of CuN_x increased with increasing Cu doping from 6.97% for 1Cu-HNCN to 13.62% for 4Cu-HNCN (Fig. S4). Thus, given the high nitrogen content in the CN matrix, Cu species can be firmly bound to the nitrogen ligand [21,53]. Furthermore, the O 1s spectra of the three catalysts showed the same O species (Fig. 2e) with binding energies of 531.8 and 532.9 eV, which were attributed to surface O-H and adsorbed H_2O, respectively [54].

HNCN and Cu-HNCN exhibited high contents of adsorbed H_2O, which was attributed to the expanded specific surface area due to the nano-tubular morphology. As shown in Fig. 2f, the peaks at 932.3 and 933.5 eV in the Cu 2p spectrum were attributed to $2p_{3/2}$ Cu(I) and Cu (II), respectively. The presence of Cu(I) was attributed to the production of reduced NH_3 during thermal polymerization. Moreover, no Cu(0) peak was found in the Cu LM2 Auger spectrum (inset of Fig. 2f), implying that all the Cu in Cu-HNCN was present as

single-electron-capacity CuN_x redox sites. Therefore, all the characterization results demonstrate that highly diffuse CuN_x sites were successfully incorporated into Cu-HNCN.

3.1.2. Photogenerated charge separation and transfer analysis

The optical absorption and charge separation/transfer behaviors of all samples were systematically studied. As shown in Fig. 3a, the light absorption edge of HNCN red-shifted, and the absorption intensity in the visible-light region increased compared with that of disordered CN, indicating that the nanotubular structure improved visible-light utilization. This finding can be attributed to the reflection of incident light in the tube, which improved light absorption [55] and can be explained by

quantum confinement effects. According to the particle-in-a-box approximation, the thinner the low-dimensional material, the stronger its confinement effect [51]. The strengthened confinement effect caused by the single-layer tube wall of HNCN can cause differences in the bandgap. Furthermore, the visible-light absorption of the Cu-CN and Cu-HNCN catalysts was significantly enhanced, which may be attributed to metal doping narrowing the bandgap of the materials. The band gap energies of Cu, Cu-CN, HNCN, and Cu-HNCN calculated using the Kubelka–Munk formula were 2.87, 2.62, 2.81, and 2.54 eV, respectively (Fig. 3b). Thus, the construction of nanotubes and the anchoring of CuN_x sites narrowed the bandgap energy of Cu-HNCN, which in turn enhanced its visible-light utilization [56]. In addition, the edge potential of
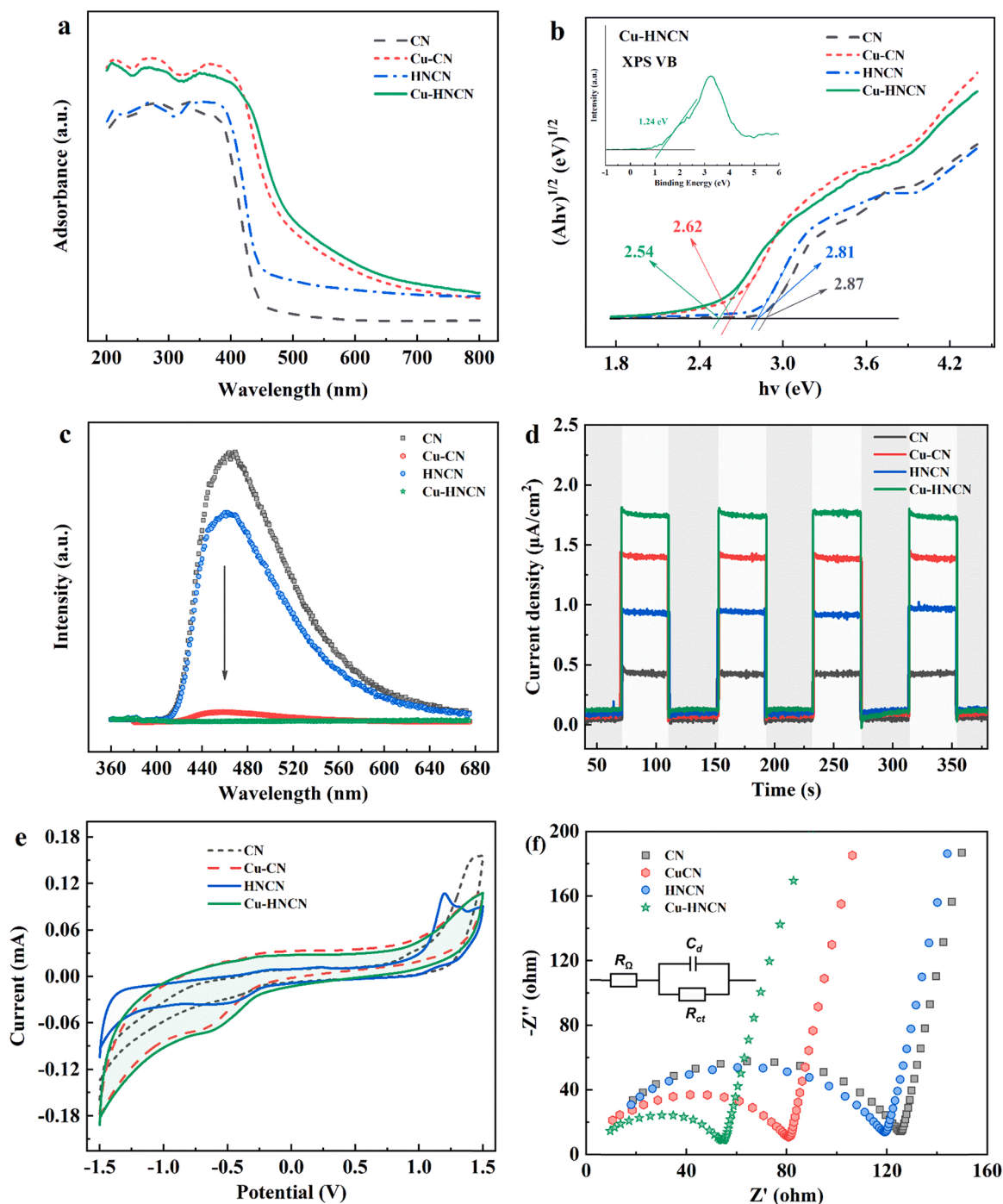
Fig. 3. (a) Ultraviolet-visible light diffusion reflectance spectra, (b) Kubelka–Munk function curves (XPS; VB spectrum, inset), (c) PL spectra, (d) transient photocurrent, (e) CV curves, and (f) Nyquist plots of CN, Cu-CN, HNCN, and Cu-HNCN.

Cu-HNCN was obtained from the XPS valence-band spectra (Fig. 3b, inset). The calculated E_{VB} was 1.24 eV, whereas the E_{CB} was −1.30 eV according to Eq. (2), indicating that O_2 can generate·O_2^- from the CB of Cu-HNCN during photocatalysis (O_2/·O_2^-: −0.33 eV), whereas H_2O cannot generate·OH directly from the VB (H_2O/·OH: 2.40 eV) [25,57].

$$E_g = E_{VB} + E_{CB} \tag{2}$$

Photoluminescence (PL) spectroscopy, photocurrent response, cyclic voltammetry (CV) curves, and electrochemical impedance spectroscopy (EIS) were used to investigate the charge separation/transport performance of the Cu-HNCN catalysts in detail. First, the original CN exhibited a distinct photocarrier recombination signal at 470 nm (Fig. 3c) [58]. The recombination signal of Cu-CN was significantly quenched, indicating that the presence of CuN_x sites inhibited the recombination of photogenerated charges. The charge recombination signal of HNCN was also suppressed compared to that of CN, and Cu-HNCN was detected with an almost completely quenched PL signal, indicating the best photogenerated charge separation performance. Fig. 3d shows the transient photocurrent response of the prepared catalysts under dark/light illumination. Cu-CN exhibited a stronger photocurrent signal than CN because of the capture of electrons by Cu (II)N_x, which facilitated the separation and transfer efficiency of photogenerated charges [59]. Moreover, Cu-HNCN exhibited the strongest photocurrent signal, indicating that the nanotubes promoted charge separation. Similar results were obtained for the CV curves and EIS analyses. As shown in Fig. 3e, Cu-HNCN exhibited the largest CV ring area, revealing its excellent charge-transfer capability. As shown in

Fig. 3f, the high-frequency regions of the Nyquist plots for all four samples show semicircles, which indicate the ohmic resistance and charge transfer impedance of the electrode–electrolyte interface [60]. Particularly, HNCN had a smaller Nyquist arc radius than CN, indicating that the nanotubes reduced the charge-transfer resistance. Cu-CN also showed a small Nyquist arc radius, indicating that the CuN_x sites improved charge transfer and conductivity. Importantly, Cu-HNCN exhibited the smallest Nyquist arc radius in the high-frequency region, indicating its excellent charge transfer and transport capabilities.

The above results prove that the anchoring of CuN_x sites and the construction of nanotubes contributed to the separation and transfer of photogenerated charges. First, the Cu(II)N_x in the CuN_x site can capture electrons and be reduced to Cu(I)N_x, which realizes effective charge separation [29,61]. Second, according to the quantum confinement effect, the reduction of the dimensionality of the semiconductor material can enhance quantization along the confinement direction, implying a large difference in the density of states in the length and diameter directions of the nanotube [62]. These differences result in a high tendency for carriers to migrate along the length of the nanotube; this migration is more efficient than disordered migration in the 2D plane of pristine CN [63]. Thus, the unique nanotube-like structure of Cu-HNCN may achieve the directional migration of electrons, which in turn enhances charge separation and transport.
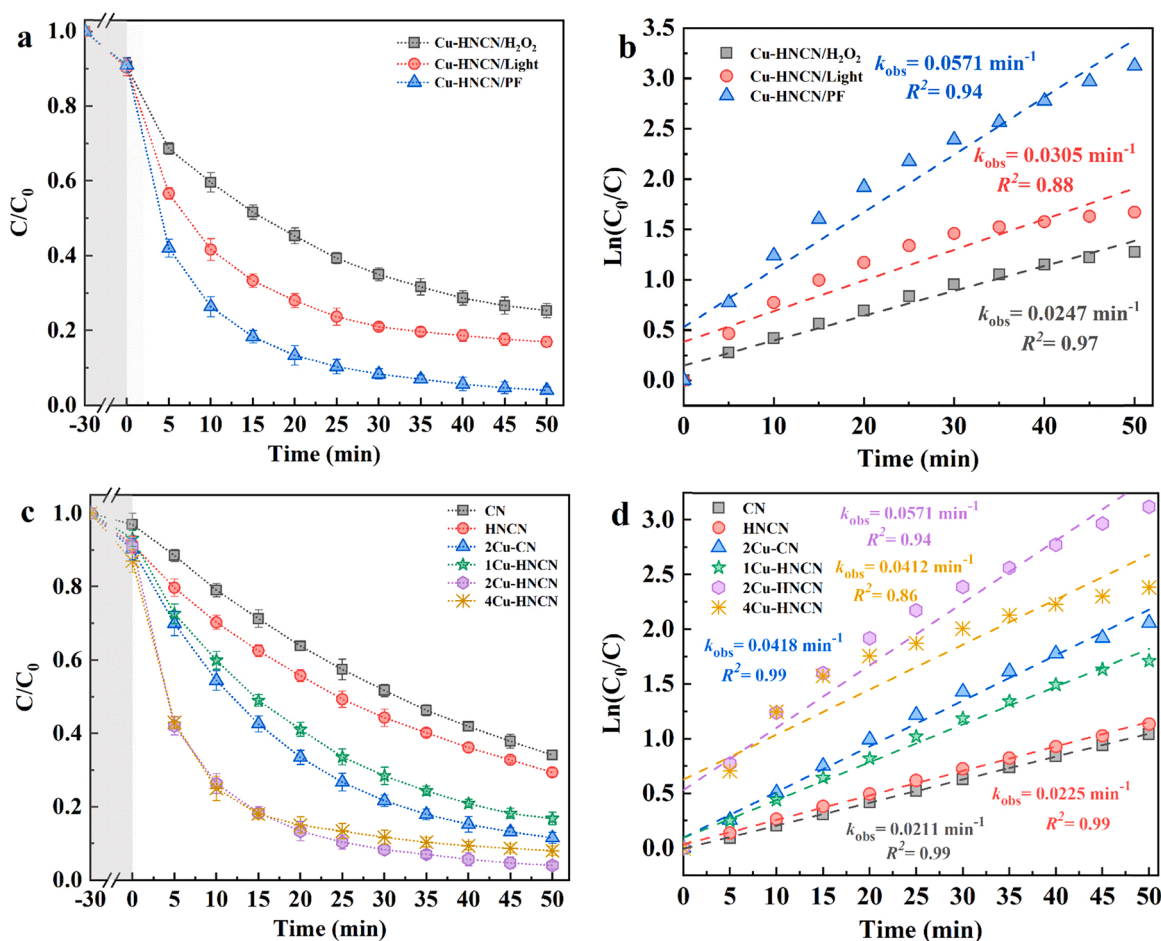

Fig. 4. (a) TET degradation with Cu-HNCN through different reaction systems. (b) Kinetics of TET degradation with Cu-HNCN through different reaction systems. (c) TET degradation with different catalysts through the PF system. (d) Kinetics of TET degradation with different catalysts through PF system (20 ℃, catalyst dosage = 0.2 g/L, H_2O_2 concentration = 20 mM, pH = 6.5, TET = 10 mg/L).

3.2. PF degradation performance

3.2.1. Effect of different systems

As shown in Fig. S5, TET barely degraded under H_2O_2, light, and H_2O_2/light without a catalyst, indicating that the homogeneous system alone cannot degrade TET. Fig. 4a shows the degradation performance of Cu-HNCN on TET in different systems. Cu-HNCN can degrade TET in the presence of H_2O_2, and the degradation efficiency reached 74.7% within 50 min, indicating that the CuN_x sites in Cu-HNCN activated H_2O_2 [16]. Under visible-light illumination, the degradation efficiency of Cu-HNCN for TET reached 83.0% within 50 min, suggesting the visible photocatalytic activity of Cu-HNCN. Notably, the TET degradation efficiency of the Cu-HNCN/PF system reached 96.0% within 50 min, with a fitted first-order kinetic rate constant (k_{obs}) of 0.0571 min^{-1} (Fig. 4b), which was higher than those of the Cu-HNCN/H_2O_2 (0.0247 min^{-1}) and Cu-HNCN/light (0.0305 min^{-1}) systems by 2.3 and 1.9 times, respectively. The excellent TET degradation performance indicated that the Cu-HNCN/PF system had good catalytic activity, which may be attributed to the intrinsic promotion mechanism of the heterogeneous Fenton-like and photocatalytic reactions [29,64]. Briefly, the Cu-HNCN catalyst was excited by visible light to generate photogenerated electrons, and owing to its excellent charge separation and transport properties, the reuse of $Cu(I)N_x$ and activation of H_2O_2 were enhanced.

Fig. 4c shows the TET degradation by the different catalysts during the PF reaction. The TET degradation efficiency of CN after 50 min was 65.9%, whereas HNCN showed higher catalytic activity with a 70.7% degradation efficiency. This result was attributed to the enlarged specific surface area and rich pore structure of HNCN, which increased the number of catalytically active sites. In addition, photoelectrochemical tests proved that HNCN possesses strong photoelectrochemical properties, which also contribute to the degradation of TET [65]. Notably, 2Cu-CN and 2Cu-HNCN with an initial Cu content of 2% exhibited enhanced TET degradation, with degradation efficiencies of 88.5% and 96.0% within 50 min, respectively. The anchoring of copper species significantly promoted TET degradation, indicating the important role of the CuN_x active sites in activating H_2O_2 during the PF process [29]. In addition, with a similar Cu content, the k_{obs} values of Cu-HNCN were significantly higher than those of Cu-CN (0.0571 min^{-1} vs. 0.0418 min^{-1}) (Fig. 4d), suggesting the role of hollow nanotubes, including the provision of a larger specific surface area, richer pores, stronger light absorption, and more efficient charge separation/transport [66]. The TET degradation efficiencies of Cu-HNCN with different Cu contents during PF were in the order 2Cu-HNCN (96.0%) > 4Cu-HNCN (92.0%) > 1Cu-HNCN (83.3%), and the corresponding k_{obs} were in the order 2Cu-HNCN (0.0571 min^{-1}) > 4Cu-HNCN (0.0412 min^{-1}) > 1Cu-HNCN (0.0346 min^{-1}). Thus, the 2Cu-HNCN catalyst was used in subsequent experiments.

3.2.2. Effect of H_2O_2 concentration, catalyst dosage, initial pH, TET concentration, coexisting substances, and water matrix

The effects of the H_2O_2 concentration, catalyst dosage, initial pH, coexisting substances, and water matrix on the degradation of TET by the Cu-HNCN/PF system were investigated to study the intrinsic linkage and applicability of the system. As shown in Fig. S6a, when the H_2O_2 concentration increased from 2.0 mM to 20 mM, the TET degradation efficiency increased from 88.4% to 96.0%, and k_{obs} increased from 0.0352 min^{-1} to 0.0571 min^{-1}. When the H_2O_2 concentration was further increased to 30 mM, the TET degradation performance showed no significant enhancement (96.7% TET degradation efficiency and 0.0627 min^{-1} k_{obs}). An appropriate increase in the H_2O_2 concentration can increase the·OH concentration, which in turn accelerates the degradation. However, excessive H_2O_2 can cause oversaturation of the reaction sites and result in the scavenging of·OH, which can inhibit degradation [67].

Fig. S6b shows the effect of the catalyst dosage. The dosage of Cu-HNCN increased from 0.05 g/L to 0.2 g/L, corresponding to an increase in TET degradation efficiency from 87.4% to 96.0% and k_{obs} from 0.0359 min^{-1} to 0.0571 min^{-1}. However, when the catalyst dosage was increased to 0.4 g/L, the degradation efficiency did not increase accordingly (95.4%), and the corresponding k_{obs} was suppressed (0.0529 min^{-1}). TET degradation was positively correlated with catalyst dosage over a certain range, confirming the role of heterogeneous reactions. Excess catalyst in the aqueous phase agglomerates and may affect the transmission of visible light, thereby affecting the PF process.

Fig. S6c shows the effect of the TET concentration. The removal efficiencies at TET concentrations of 5, 10, 20, and 40 mg/L were 97.2%, 96.0%, 94.6%, and 90.1%, respectively. The TET removal efficiency decreased with increasing TET concentrations. The number of active species produced in the system was approximately constant for the same operating parameters. Therefore, more active species are required for the degradation of high concentrations of pollutants.

Fig. 5a shows the effect of different initial pH values on TET degradation. The pH of the TET solution without HCl or NaOH treatment is 6.5. Overall, the TET degradation efficiencies at pH = 6.5, 3, 4, 5, 6, 7, 8 9 were 96.0%, 68.3%, 92.4%, 95.4%, 96.1%, 94.9%, 88.9%, and 71.6%, respectively, corresponding to k_{obs} of 0.0571, 0.0226, 0.0503, 0.0570, 0.0552 0.0522, 0.0382, and 0.0206 min^{-1}. The degradation of TET at pH = 3 was severely inhibited, and this was attributed to the introduction of Cl^- by HCl, which in turn scavenged·OH to produce the less oxidizable·$ClOH^-$ [68]. By contrast, the TET degradation efficiency was significantly higher at pH = 4. Therefore, the weak TET degradation under strong acidity was not solely due to the quenching effect of Cl^-. The zero-point charge of Cu-HNCN measured using the zeta potentiometer was 4.3 (Fig. S7), indicating positive and negative potentials on the catalyst surface at pH < 4.3 and pH > 4.3, respectively. Meanwhile, TET is mainly present as TCH^{3+} at pH < 3.3 and as TCH^- and TC^{2-} at pH > 7.7 [3]. Thus, the electrostatic repulsion between the catalyst surface and TCH^{3+} under strong acidity also inhibits TET degradation. In addition, electrostatic repulsion exists under alkaline conditions, and the additional decomposition of H_2O_2 can inhibit the PF process [69].

Fig. 5b shows the effect of inorganic anions (including Cl^-, NO_3^-, CO_3^{2-}, HPO_4^{2-}, and SO_4^{2-}) on the degradation of TET. At a Cl^- concentration of 20 mM, the TET degradation efficiency was reduced to 88.1%, which was attributed to the low oxidation capacities of·$ClOH^-$ and·Cl^-. The presence of NO_3^- had a negligible effect (92.9% degradation efficiency in 50 min) owing to the generation of the·NO_3 oxidant [70]. The inhibitory effect was significant in the presence of CO_3^{2-}, and the degradation efficiency of TET decreased to 79.7% at a concentration of 20 mM. CO_3^{2-} can produce HCO_3^- and H_2CO_3 in water to increase the pH of the reaction solution and act as scavengers of·OH [71]. HPO_4^{2-} also exhibited an inhibitory effect, and the degradation efficiency of TET at 20 mM decreased to 80.3%, which was attributed to the formation of HPO_4·with·OH or the increase in solution pH. Remarkably, the TET degradation efficiency was not inhibited in the presence of SO_4^{2-}, reaching 96.3% at 20 mM SO_4^{2-} owing to the generation of the strong oxidant·SO_4^{2-} [72]. Humic acid was selected as typical natural organic matter (NOM) to investigate the effect of NOM on the degradation process. As shown in Fig. 5c, when the HA concentration increased from 3 to 10 mg/L, the degradation efficiency decreased from 89.9% to 82.5%, and k_{obs} decreased from 0.0381 min^{-1} to 0.0286 min^{-1}. The addition of HA inhibited the degradation of TET owing to the additional consumption of radicals by HA. Moreover, the phenolic hydroxyl and carboxyl groups of HA could be adsorbed on the Cu-HNCN surface, shielding the reaction sites.

The degradation of TET by the Cu-HNCN/PF system in real water bodies was investigated using River A and Lake B as the water matrix (Fig. 5d); the chemical oxygen demand (COD), total nitrogen (TN), and total phosphorus (TP) of River A were lower than those of Lake B, which was attributed to the improved self-purification capability of flowing water bodies [73]. Compared with the ultrapure water matrix, the TET degradation efficiency in River A and Lake B declined to 89.2% and
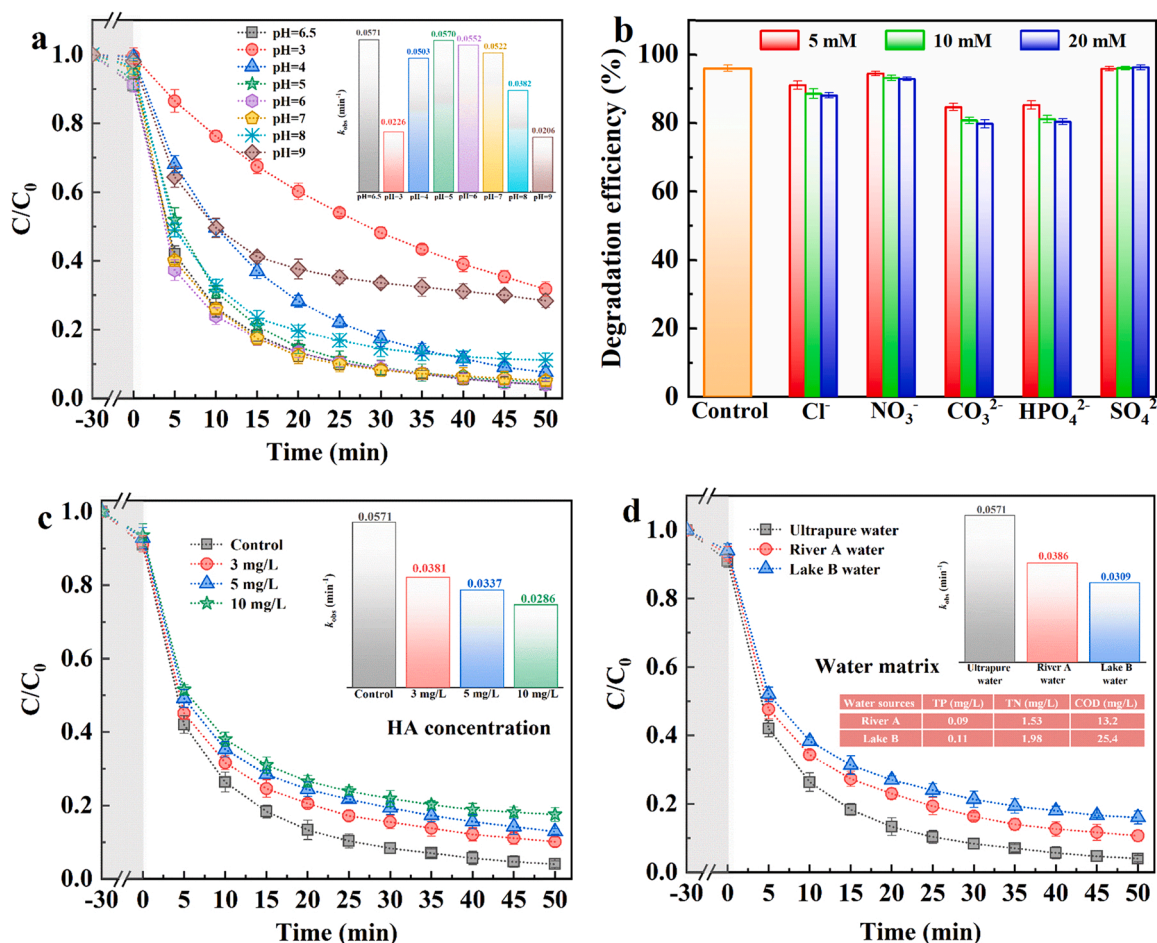
Fig. 5. (a) Effect of initial pH on TET degradation with Cu-HNCN/PF system (20 ℃, catalyst dosage = 0.2 g/L, H_2O_2 concentration = 20 mM, TET = 10 mg/L). (b) Effect of inorganic ions on TET degradation with Cu-HNCN/PF system (20 ℃, catalyst dosage = 0.2 g/L, H_2O_2 concentration = 20 mM, TET = 10 mg/L). (c) Effect of NOM on TET degradation with Cu-HNCN/PF system (20 ℃, catalyst dosage = 0.2 g/L, H_2O_2 concentration = 20 mM, pH = 6.5, TET = 10 mg/L). (d) Effect of different water sources on TET degradation with Cu-HNCN/PF system (20 ℃, catalyst dosage = 0.2 g/L, H_2O_2 concentration = 20 mM, TET = 10 mg/L).

84.2%, respectively. The degradation of TET was influenced by the real water matrix, which was closely related to the presence of anions, NOM, and bacteria in real water bodies. These components compete with pollutants for active sites and radicals. Overall, the Cu-HNCN/PF system maintained the TET degradation capacity (more than 80% degradation efficiency) in real complex water bodies. Table S3 summarizes the reported degradation of TET via photocatalytic and Fenton-like reactions. The Cu-HNCN-mediated PF process demonstrated stronger TET removal and faster catalytic reaction rate than the photocatalytic and Fenton-like processes with a lower catalyst dosage, revealing the advantage of the Cu-HNCN/PF system for TET degradation.
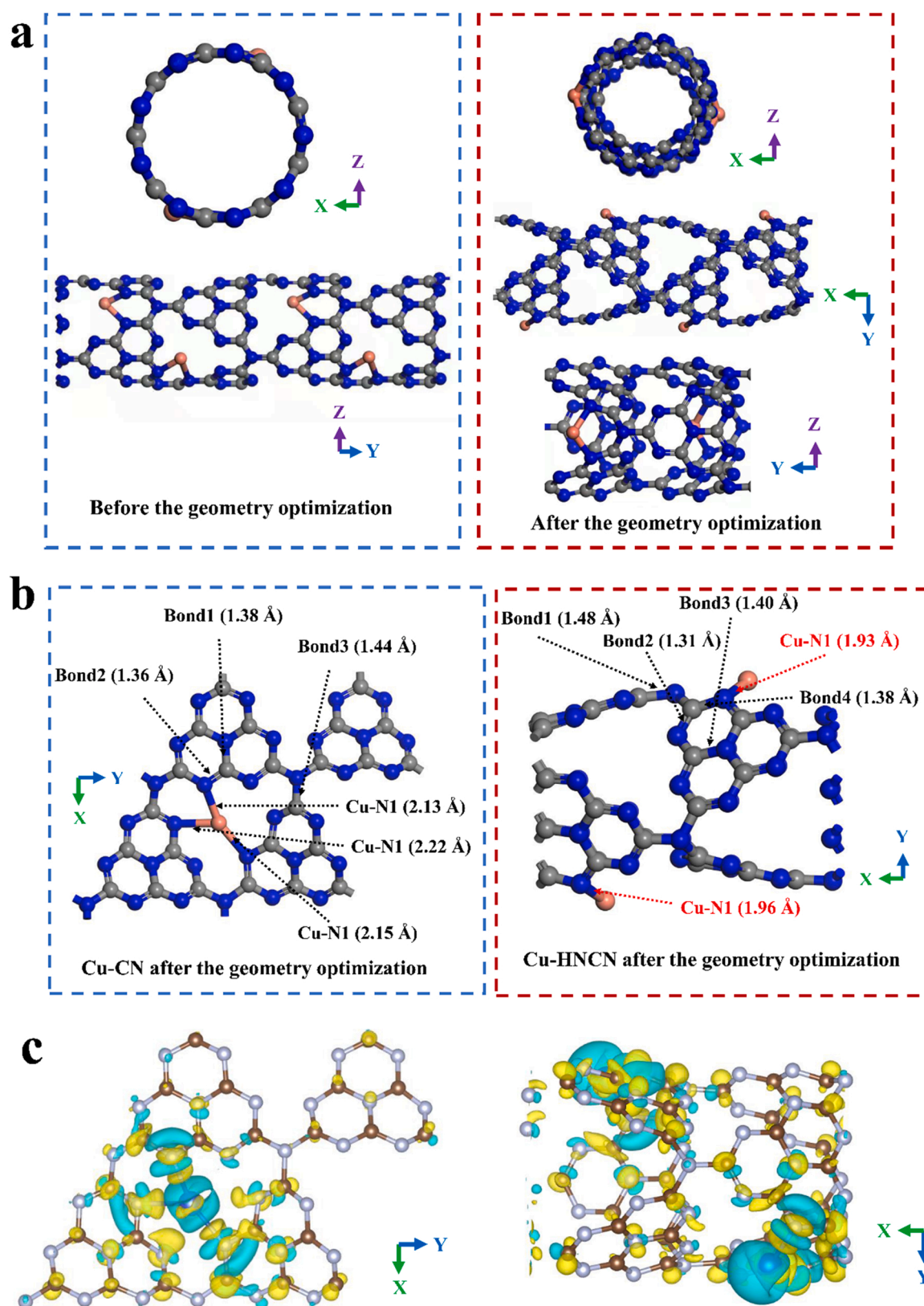
3.3. Geometric optimization and DFT calculation

Atomic models of planar Cu-CN and nanotube Cu-HNCN were developed and their structures were optimized. As shown in Fig. 6a and b, the bond lengths and angles of the geometrically optimized nanotube atomic models changed to reach the most stable state. Compared with the planar model, the bond lengths between the C and N atoms in the nanotubes appeared different, and the change in bond length led to a change in bond energy, which is consistent with the XPS results. Emphatically, compared with 2.13–2.22 Å in the planar model, the Cu-N bond length in the nanotubes was significantly shortened to 1.93–1.96 Å due to the bending of the planes. In general, short Cu-N bonds exhibit strong interactions and high bond energies, which may stabilize Cu in Cu-HNCN [74].

The differential charge density was calculated to investigate the effect of nanotubes on charge transport. As shown in Fig. 6c, the yellow region represents charge enrichment, and the blue region represents charge depletion. The nanotube atom model demonstrated high density and large areas of charge enrichment and depletion, suggesting that the model was beneficial for charge separation and transport [23]. Therefore, the differential charge density calculation results confirmed that Cu-HNCN exhibited enhanced charge separation and transport performance compared to planar Cu-CN. In addition, a large region of charge depletion around the Cu atom was observed in the nanotube model. The short Cu-N bond length caused by the nanotubes means that the electronegativity difference between Cu and N atoms increases, resulting in a large attraction difference between Cu and N for electrons, which could increase the tendency of electron enrichment in the Cu-adjacent N atoms.

3.4. Stability study

The reusability of the Cu-HNCN and Cu-CN catalysts was investigated (Fig. 7a). After 10 cycles of reuse, the TET degradation efficiencies of Cu-HNCN and Cu-CN in the PF process decreased from 96.0% and 88.5–82.9% and 68.7%, respectively. The decrease in the degradation efficiency was attributed to the shielding of the active sites by the intermediates. The catalytic activity was reset after the catalysts were fully washed, dried, and annealed at 550 ℃ for 1 h. The TET degradation efficiencies of the recovered Cu-HNCN and Cu-CN catalysts declined

a

Before the geometry optimization

After the geometry optimization

b

Bond1 (1.38 Å)

Bond3 (1.44 Å)

Bond2 (1.36 Å)

Cu-N1 (2.13 Å)

Cu-N1 (2.22 Å)

Cu-N1 (2.15 Å)

Cu-CN after the geometry optimization

Bond3 (1.40 Å)

Bond1 (1.48 Å)

Bond2 (1.31 Å)

Cu-N1 (1.93 Å)

Bond4 (1.38 Å)

Cu-N1 (1.96 Å)

Cu-HNCN after the geometry optimization

c

Fig. 6. (a) Atomic model of the Cu-HNCN before and after geometric optimization. (b) Atomic model of Cu-CN and Cu-HNCN after geometric optimization and the corresponding bond length. (c) Calculated charge density difference of Cu-CN and Cu-HNCN (the yellow and cyan areas indicate charge accumulation and depletion, respectively).
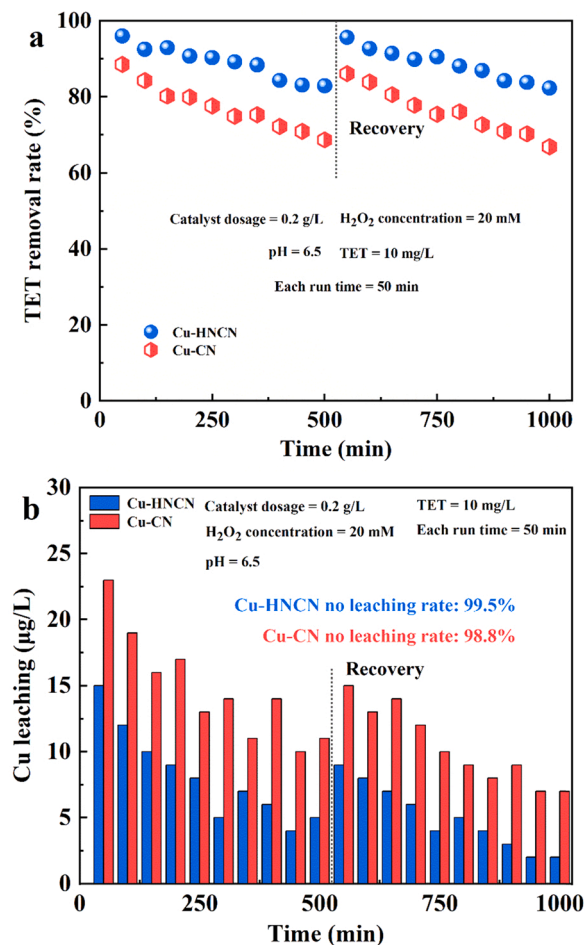
Fig. 7. (a) TET removal by Cu-HNCN and Cu-CN under PF reaction in 20 cycles (20 ℃, catalyst dosage = 0.2 g/L, H_2O_2 concentration = 20 mM, pH = 6.5, TET = 10 mg/L). (b) Cu leaching amounts of Cu-HNCN and Cu-CN in each cycle (20 ℃, catalyst dosage = 0.2 g/L, H_2O_2 concentration = 20 mM, pH = 6.5, TET = 10 mg/L).

from 95.6% and 86.1–82.3% and 66.9%, respectively, over 10 cycles. Cu-HNCN showed slight inhibition of TET degradation, which could be related to the stable CuN_x sites. The Cu concentration remaining in the solution with Cu-HNCN was significantly lower than that of Cu-CN (Fig. 7b), and the Cu retention of Cu-HNCN after 20 cycles was 99.5%. The short Cu-N bonds (1.93–1.96 Å) of Cu-HNCN obtained from DFT calculations further stabilized the catalyst, revealing that nanotubes can improve catalyst stability.
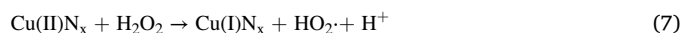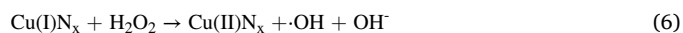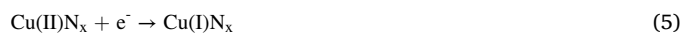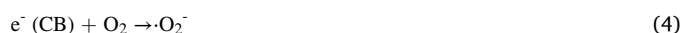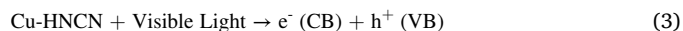
Furthermore, the XRD patterns showed that the (002) crystal plane of Cu-HNCN exhibited a good characteristic diffraction after cycling (Fig. S8a), indicating that Cu-HNCN can maintain its structural stability during long-term operation. The retained Cu-HNCN nanotubes were confirmed by SEM images (Fig. S8b and c). Fig. S8d shows the Cu 2p spectra of the fresh and recycled catalysts. The $2p_{3/2}$ Cu(I)/$2p_{3/2}$ Cu(II) content in Cu-HNCN before and after use decreased slightly from 79.75/20.25 to 77.23/22.77. The valence state of Cu was maintained owing to the excellent photogenerated charge separation and transport performance of Cu-HNCN, which allowed the effective reduction of Cu(I) after the activation of H_2O_2 to form Cu(II). The above results further indicate that Cu-HNCN possesses good stability, which provides a reference for the application of this catalyst in complex water purification.

### 3.5. Mechanism of PF degradation

3.5.1. Identification of radical species

As a typical free radical in Fenton-like reactions, ·OH has been studied for the first time. Isopropyl alcohol (IPA) was used as an·OH scavenger, and the results are shown in Fig. 8a. When the IPA concentration increased from 5 mM to 100 mM, the TET degradation efficiency decreased from 89.8% to 84.7%, indicating that·OH was an important radical for TET degradation. Benzoquinone (BQ) was used as a quencher for·O_2^- to investigate the role of·O_2^- in the PF process. As shown in Fig. 8b, the degradation efficiency of TET declined from 91.6% to 74.1% when the BQ concentration was increased from 0.05 mM to 0.2 mM. The TET degradation was significantly inhibited by the scavenging of·O_2^-, proving that·O_2^- was the dominant radical in the Cu-HNCN/PF system. The contribution of h^+ ions to the degradation of TET was also investigated. As shown in Fig. 8c, when the concentration of triethanolamine (TEOA) increased from 25 mM to 100 mM, the TET degradation efficiency decreased from 88.5% to 82.4%. In addition, the roles of electron and non-radical ROS were probed using $AgNO_3$ and histidine (L-His) as electron and $^1O_2$ scavengers, respectively (Fig. 8d and e). The efficiency of TET degradation after complete quenching of electrons and $^1O_2$ decreased to 91.9% and 89.2%, respectively. The results of quenching experiments showed that·OH,·O_2^-, h^+, e^-, and $^1O_2$ played a role in TET degradation. Fig. 8f summarizes the inhibition of k_{obs} in the Cu-HNCN/PF system by quenching all radicals and non-radical ROS. The results showed that the main free species responsible for TET degradation were·O_2^- and h^+ (inhibition of k_{obs} reached 64.1% and 48.7%, respectively) and that·OH also played an important role (inhibition of k_{obs} was 45.3%). Notably, $^1O_2$ inhibited k_{obs} by 31.1%, suggesting that it was a non-radical ROS for TET degradation.

The dominant role of·O_2^- and h^+ in the PF reaction was attributed to the excellent visible-light utilization and capability to separate photogenerated electron-hole pairs in the Cu-HNCN catalyst [11,75]. The CB of Cu-HNCN accumulated large numbers of photogenerated electrons, which in turn reacted with O_2 on the catalyst surface to form·O_2^- (as demonstrated in Section 3.1.2) (Eqs. (3–4)). Electrons were fully consumed owing to the generation of·O_2^- and participation in the valence cycle of Cu(I/II) (Eqs. (4–5)). Thus, the h^+ of the VB of Cu-HNCN was released to participate in TET degradation. The important role of·OH was attributed to the efficient activation of H_2O_2 by the Cu-HNCN catalyst (Eqs. (6–7)). In addition, $^1O_2$ production was due to the reaction of abundant·O_2^- in the system with H^+, H_2O, and·OH (Eqs. (8–10)) [76].

$$Cu\text{-}HNCN + Visible\ Light \rightarrow e^- (CB) + h^+ (VB) \tag{3}$$

$$e^- (CB) + O_2 \rightarrow \cdot O_2^- \tag{4}$$

$$Cu(II)N_x + e^- \rightarrow Cu(I)N_x \tag{5}$$

$$Cu(I)N_x + H_2O_2 \rightarrow Cu(II)N_x + \cdot OH + OH^- \tag{6}$$

$$Cu(II)N_x + H_2O_2 \rightarrow Cu(I)N_x + HO_2 \cdot + H^+ \tag{7}$$

$$\cdot O_2^- + \cdot O_2^- + 2H^+ \rightarrow {}^1O_2 + H_2O_2 \tag{8}$$

$$\cdot O_2^- + \cdot O_2^- + H_2O \rightarrow 1 \cdot 5^1O_2 + 2OH^- \tag{9}$$

$$\cdot O_2^- + \cdot OH \rightarrow {}^1O_2 + OH^- \tag{10}$$

The production of·OH was semi-estimated by electron paramagnetic resonance (EPR) using DMPO as a trapping agent. As shown in Fig. 9a, Cu-HNCN and Cu-CN had four distinctive 1:2:2:1 characteristic peaks of DMPO-·OH adducts during the PF reaction [77], indicating that H_2O_2 was activated by the copper species. In particular, the stronger signal intensity of DMPO-·OH in the Cu-HNCN/PF system suggests that H_2O_2 was effectively activated by Cu-HNCN, proving the positive role of nanotubes in TET degradation. The generation of·OH from Cu-HNCN in the different reaction systems was also compared. As shown in Fig. 9b, Cu-HNCN/PF exhibited a more pronounced DMPO-·OH signal than the
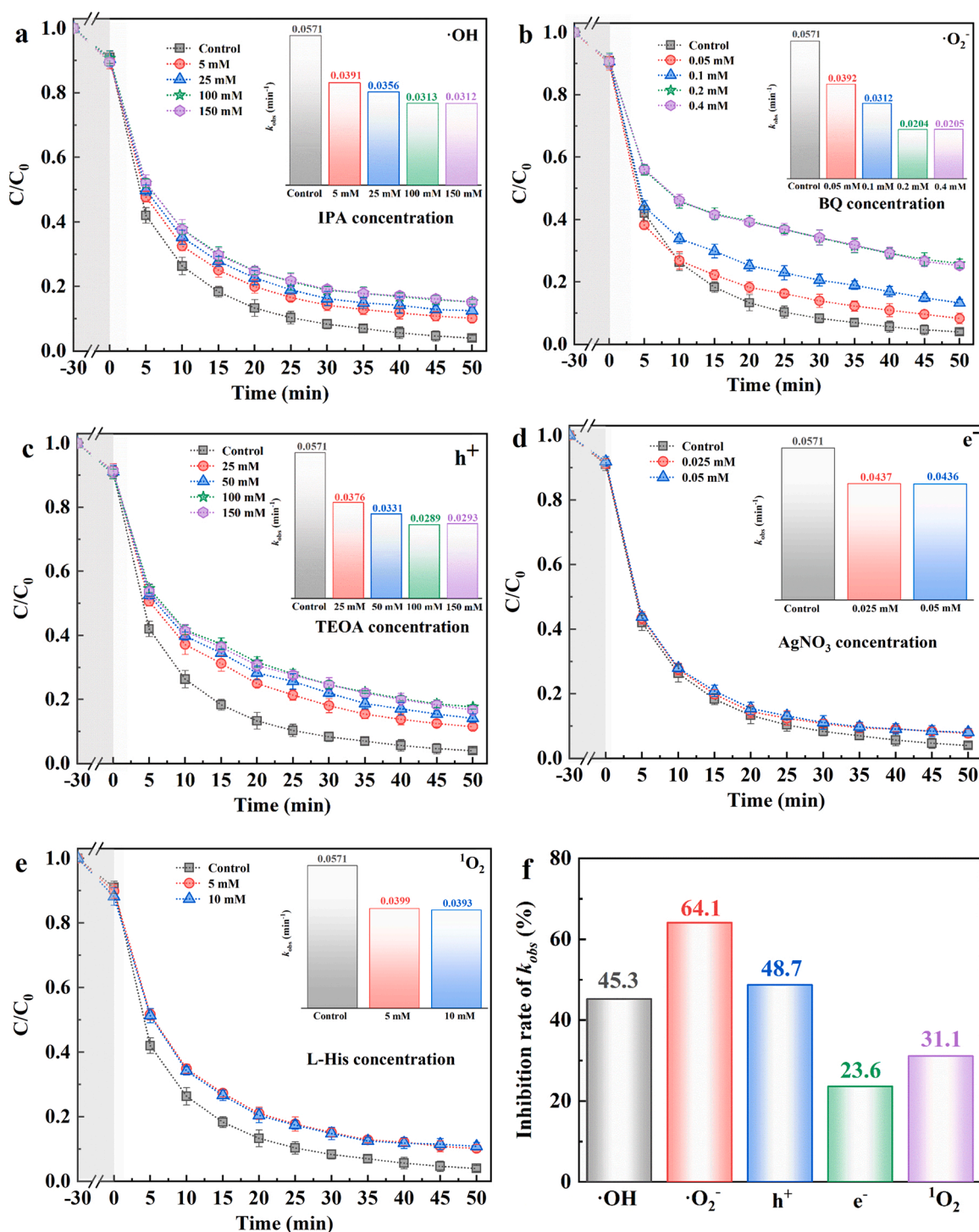
Fig. 8. (a) Effect of radical scavengers on TET degradation with Cu-HNCN/PF system: (a) IPA, (b) BQ, (c) TEOA, (d) AgNO$_3$, and © L-His (20 ℃, catalyst dosage = 0.2 g/L, H$_2$O$_2$ concentration = 20 mM, pH = 6.5, TET = 10 mg/L). (f) Inhibition rate of k_{obs} by different radicals (Inhibition rate of k_{obs} (%) = 1- k_{obs}/k_{obs0}).

Cu-HNCN/H$_2$O$_2$ system, indicating that visible light promoted the activation of H$_2$O$_2$. Further, the decomposition efficiency of H$_2$O$_2$ was investigated. As shown in Fig. S9, the decomposition efficiency of H$_2$O$_2$ in Cu-HNCN/PF reached 85.7% within 50 min, which was higher than those of the Cu-CN/PF (71.1%) and Cu-HNCN/H$_2$O$_2$ (62.4%) systems. The decomposition of H$_2$O$_2$ is directly related to the amount of·OH in the system; thus, the Cu-HNCN/PF system demonstrated enhanced H$_2$O$_2$ activation capacity [78]. This result indicates that the nanotubes and visible-light illumination enhanced the activation of H$_2$O$_2$. The efficient

charge separation/transport of nanotubes under visible light can promote Cu(I) regeneration and H$_2$O$_2$ activation (Eqs. (5–6)).

In addition, the generation of·O$_2^-$ and ^{1}O$_2$ in the Cu-HNCN/PF and Cu-CN/PF systems was detected. As shown in Fig. 9c and d, quadruplet 1:1:1:1 DMPO-·O$_2^-$ and triplet 1:1:1 TEMP-^{1}O$_2$ adduct signals appeared, demonstrating the presence of both in the PF process [79]. Moreover, the stronger adduct signal in Cu-HNCN/PF indicates that Cu-HNCN produced higher concentrations of·O$_2^-$ and ^{1}O$_2$. The enhanced visible-light absorption and charge separation properties of Cu-HNCN
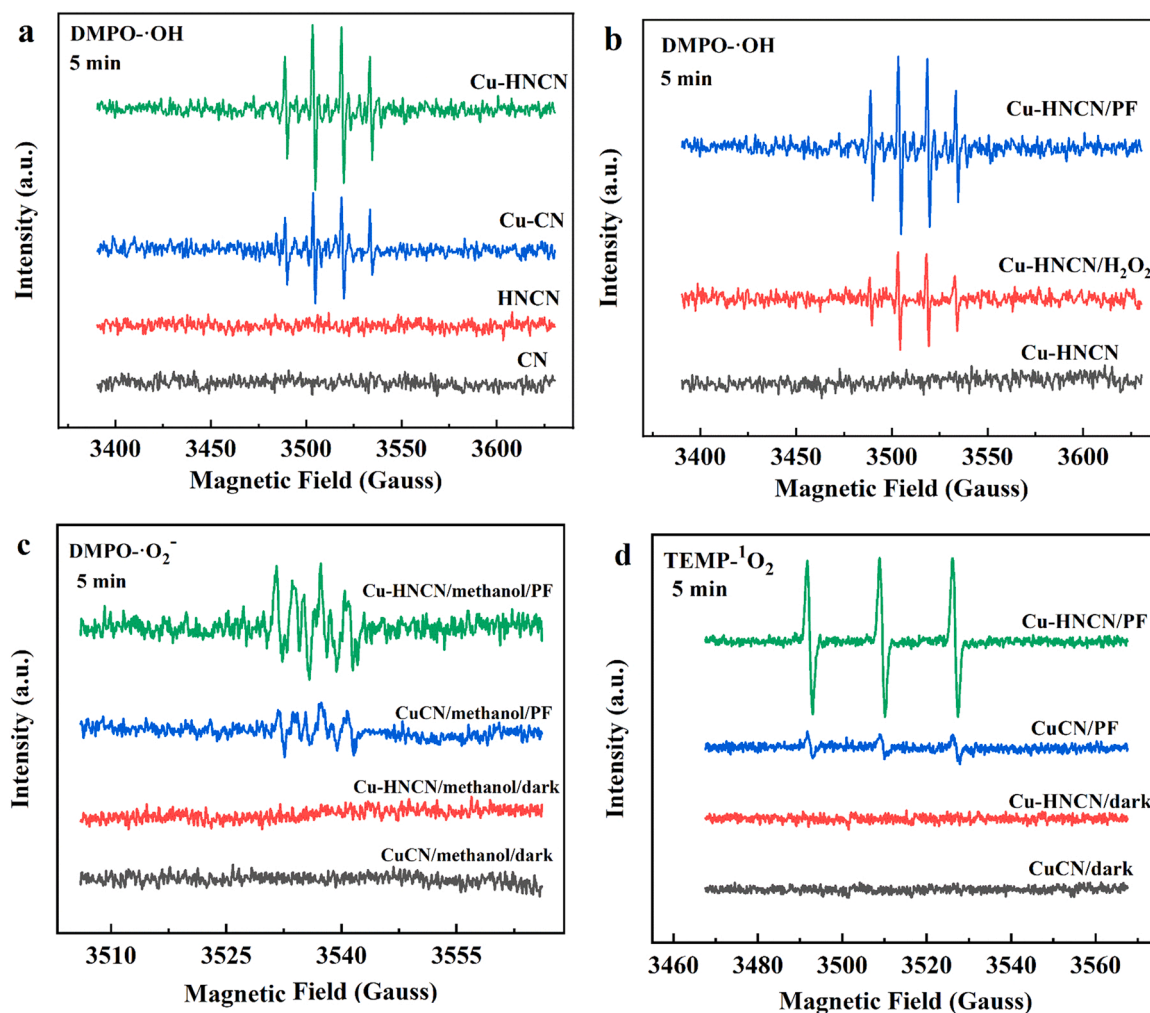
Fig. 9. (a) EPR spectra of DMPO-·OH in the PF reaction with different catalysts (20 °C, catalyst dosage = 0.2 g/L, H_2O_2 concentration = 20 mM, pH = 6.5, TET = 10 mg/L). (b) EPR spectra of DMPO-·OH obtained using Cu-HNCN with different systems (20 °C, catalyst dosage = 0.2 g/L, H_2O_2 concentration = 20 mM, pH = 6.5, TET = 10 mg/L). EPR spectra for (c) DMPO-·O_2^- and (d) TEMP-$^1O_2$ in the PF reaction with different catalysts (20 °C, catalyst dosage = 0.2 g/L, H_2O_2 concentration = 20 mM).

can release more photogenerated electrons to generate·O_2^- (Eqs. (3) and (4)), whereas the more abundant·O_2^- can be accompanied by the generation of more $^1O_2$ (Eqs. (8–10)).

3.5.2. Mechanism of Cu-HNCN/PF system

The k_{obs} inhibition by Cu-HNCN/light and Cu-HNCN/H_2O_2 compared with that of the Cu-HNCN/PF system was calculated. Fig. S10 exhibits that the inhibition values of k_{obs} for TET degradation were 46.6% and 56.7% for the Cu-HNCN/light and Cu-HNCN/H_2O_2 systems, respectively, suggesting that the photocatalytic system had faster TET removal efficiency than the Fenton-like system in the presence of H_2O_2 only. This result indicates that nanotube morphology is crucial for the removal of pollutants, particularly for the enhancement of the photocatalytic activity of the PF system.

Based on the above discussion, the mechanism of TET degradation by the Cu-HNCN/PF system is summarized in Scheme 2. First, nanotube construction can enhance visible-light utilization, charge separation, and transport, whereas the additional generated and separated photogenerated electrons can react with O_2 to form·O_2^- and concomitantly produce $^1O_2$. Second, photogenerated electrons are generated and transported to achieve the effective reuse of Cu(I), which in turn enhances the activation of H_2O_2 to produce·OH. Moreover, the electrons are effectively separated and utilized to release a large amount of h^+. Additionally, the expanded specific surface area and highly exposed

active sites of the nanotubes promoted redox reactions. Ultimately, the abundance of active species (·O_2^-,·OH, h^+, and $^1O_2$) in the system and nanotube properties enable efficient degradation of TET.

Fig. S11 shows the changes in the total organic carbon (TOC) content during TET degradation. The TOC removal rate of Cu-HNCN/PF reached 60.2% within 50 min, suggesting that TET was effectively mineralized. Ofloxacin and norfloxacin were used as model contaminants to examine the oxidative selectivity of the Cu-HNCN/PF system. As shown in Fig. S12, the Cu-HNCN/PF system achieved 89.7% and 86.7% removal of ofloxacin and norfloxacin, respectively, within 50 min, while the mineralization rates were 42.1% and 37.4%, respectively, indicating that the Cu-HNCN/PF system has the potential to degrade refractory organic pollutants without selectivity. Importantly, the Cu-HNCN catalyst demonstrated better catalytic activity, especially with a faster reaction rate (0.0571 min^{-1} k_{obs}), at a lower H_2O_2 dosage than other previously reported PF systems (Table S4), revealing the superiority of the Cu-HNCN catalyst for the removal of persistent organic pollutants.

3.6. Degradation pathways analysis

The oxidative degradation behavior of TET was predicted using the FED theory. Fig. 10a–c show the optimized TET molecular conformations and FEDs of TET with the highest occupied molecular orbital (HOMO) and lowest unoccupied molecular orbital (LUMO). Fig. 10d
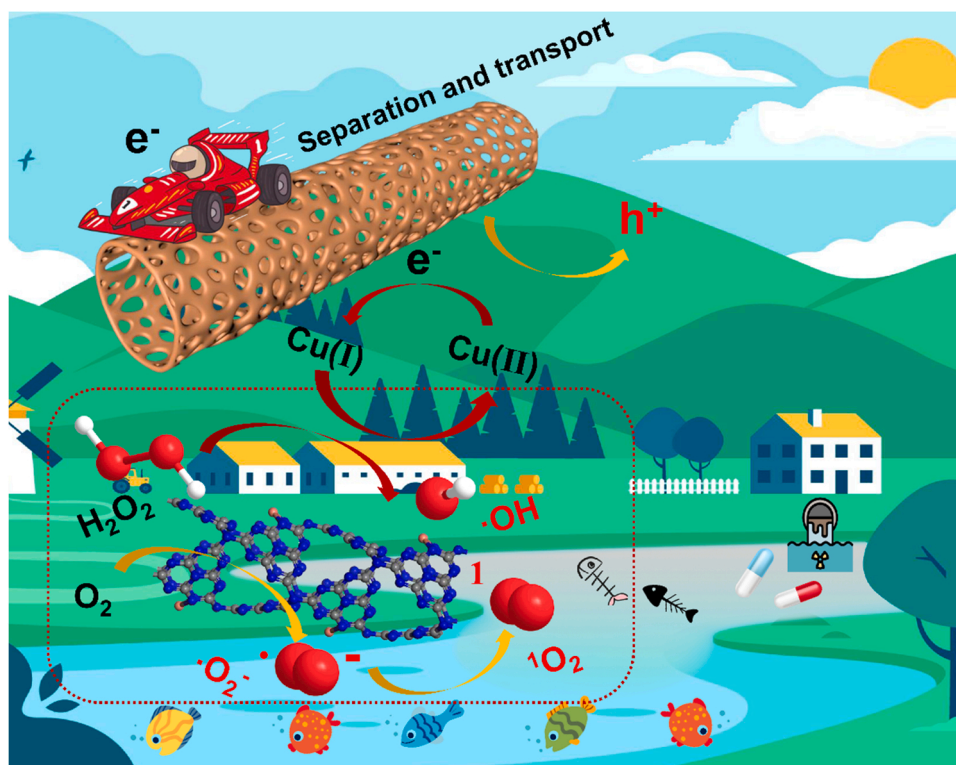
Scheme 2. Proposed TET degradation mechanism by the Cu-HNCN/PF system.

shows the details of these calculations. In general, atoms with high FED^2_{HOMO} values are electronically extracted during electrophilic reactions, whereas those with high $FED^2_{HOMO} + FED^2_{LUMO}$ values are susceptible to ROS attack [80]. Notably, 10(C), 12(C), 13(C), 14(C), and 27(O) exhibited high FED^2_{HOMO} values, indicating that benzene rings containing 10(C), 12(C), 13(C), 14(C), and -OH, including 27(O), can be oxidized by h^+. Moreover, high values of $FED^2_{HOMO} + FED^2_{LUMO}$ were observed for 1(C), 2(C), 3(C), 23(O), and 29(O), indicating that -C_1-C_2 = , -C_2 =C_3-, -C_1 =O_{23}, and C_3-O_{29}H are easily attacked by·O_2^-,·OH, and $^1O_2$.
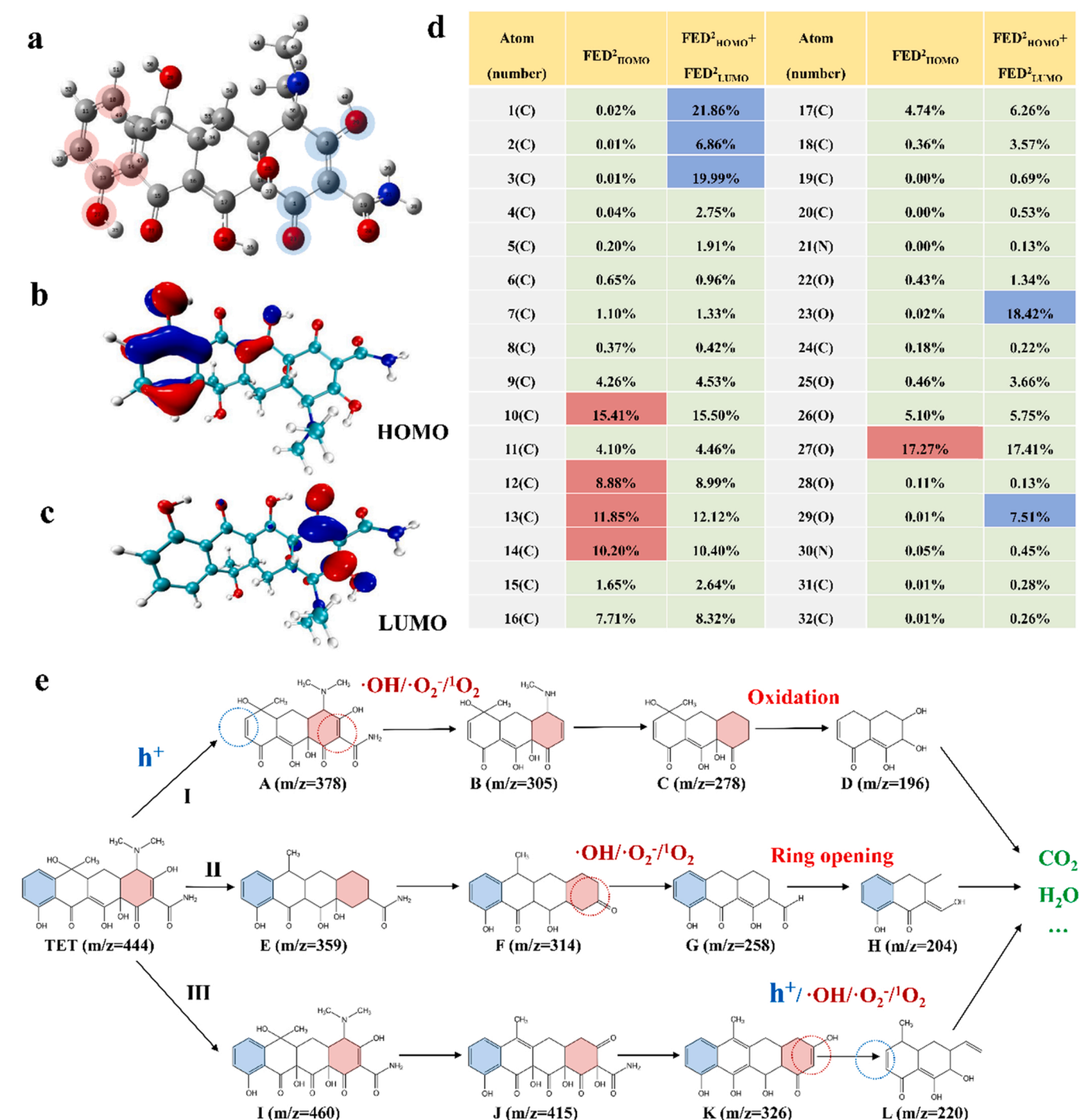
Fig. S13 shows the LC-MS spectra of the intermediates during TET degradation, and Table S5 summarizes the mass-charge (m/z) signals of all intermediates. Thus, a possible TET degradation pathway can be proposed based on the FED calculation and the m/z signal. According to pathway I, the benzene ring in TET containing 10(C), 12(C), 13(C), and 14(C) atoms was first oxidized by h^+, and the ring opened to produce A ($m/z = 378$). C_3-O_{29}H, an amide group, and N-methyl were further attacked by·O_2^-,·OH, and $^1O_2$ to produce B ($m/z = 305$). C ($m/z = 278$) and D ($m/z = 196$) were obtained by demethylation, dehydration, and ring-opening. In pathway II, -C_1 =O_{23} and C_3-O_{29}H were attacked by free species, and E ($m/z = 359$) and F ($m/z = 314$) were generated through de-N-methyl and dehydration. Then, under the attack of·O_2^-,·OH, and $^1O_2$, -C_1-C_2 = and -C_2 =C_3- belonging to the benzene ring were oxidatively ring open to form G ($m/z = 258$) and H ($m/z = 204$), respectively. In pathway III, TET was converted to I ($m/z = 460$) by the addition of a hydroxyl group and then converted to J ($m/z = 415$) based on hydroxylation, de-N-methylation, and dehydration [81]. K ($m/z = 326$) was obtained via deamidation, hydroxylation, and dehydration. The benzene rings, including 10(C), 12(C), 13(C), 14(C), and -C_1-C_2 = , -C_2 =C_3- were oxidized by h^+ and·O_2^-/·OH/$^1O_2$, and the ring opened to form L ($m/z = 220$). Finally, all intermediates, such as CO_2 and H_2O, are further mineralized into smaller molecules.

In addition, the toxicity of the intermediates in the TET degradation process needs to be monitored to exclude environmental risks. Respirometry can provide sensitive and direct access to the toxicity of

contaminants in activated sludge [82]. According to the results of microbial respiration inhibition experiments (Fig. S14), the oxygen uptake of Control 2 reached 257.64 mg/L after 24 h of incubation, whereas the original TET solution significantly inhibited the respiration of activated sludge, with an oxygen uptake of 36.83 mg/L. The oxygen uptake of the Cu-HNCN/PF system-treated TET solution increased to 157.32 mg/L, indicating that the biotoxicity of the TET was reduced by the Cu-HNCN/PF system. The calculated bio-inhibition coefficient (I_r) values of 0.88 and 0.39 for the TET and treated TET groups, respectively, indicated that the biotoxicity of TET treated with Cu-HNCN/PF system was reduced by 56%, thus demonstrating that the Cu-HNCN/PF system can effectively reduce the environmental risk posed by persistent pollutants.

4. Conclusion

In this study, Cu-HNCN nanotube catalysts with highly dispersed and stable CuN_x sites were successfully constructed and applied to degrade antibiotic contaminants by the PF process. The catalyst exhibited excellent degradation performance without selectivity for complex water matrices. Stability studies confirmed that the CuN_x sites were stably confined to the geometrically optimized Cu-HNCN because of planar bending caused by the nanotubes, which in turn led to short Cu-N bonds. Differential charge calculations indicated that the nanotubes enhanced the charge transfer. In addition, mechanistic investigation concluded that the excellent catalytic degradation capability was attributed to the nanotube properties, which enhanced the generation, separation, and transport of photogenerated electrons in Cu-HNCN, promoting the production of·O_2^-,·OH, h^+, and $^1O_2$. Moreover, based on FED calculations and LC-MS results, TET degradation pathways were proposed. Furthermore, the Cu-HNCN/PF system could effectively reduce the environmental risks caused by persistent pollutants. In summary, this study provides a new approach for improving the stability and accelerating the electron transfer of catalysts, while also providing a reference for the development of environmental functional materials

Atom (number)	FED²HOMO	FED²HOMO+ FED²LUMO	Atom (number)	FED²HOMO	FED²HOMO+ FED²LUMO
1(C)	0.02%	21.86%	17(C)	4.74%	6.26%
2(C)	0.01%	6.86%	18(C)	0.36%	3.57%
3(C)	0.01%	19.99%	19(C)	0.00%	0.69%
4(C)	0.04%	2.75%	20(C)	0.00%	0.53%
5(C)	0.20%	1.91%	21(N)	0.00%	0.13%
6(C)	0.65%	0.96%	22(O)	0.43%	1.34%
7(C)	1.10%	1.33%	23(O)	0.02%	18.42%
8(C)	0.37%	0.42%	24(C)	0.18%	0.22%
9(C)	4.26%	4.53%	25(O)	0.46%	3.66%
10(C)	15.41%	15.50%	26(O)	5.10%	5.75%
11(C)	4.10%	4.46%	27(O)	17.27%	17.41%
12(C)	8.88%	8.99%	28(O)	0.11%	0.13%
13(C)	11.85%	12.12%	29(O)	0.01%	7.51%
14(C)	10.20%	10.40%	30(N)	0.05%	0.45%
15(C)	1.65%	2.64%	31(C)	0.01%	0.28%
16(C)	7.71%	8.32%	32(C)	0.01%	0.26%

Fig. 10. (a) Optimized TET molecular configuration. (b) FEDs of HOMO of TET. (c) FEDs of LUMO of TET. (d) FEDs on atoms of TET. (e) Proposed pathways of TET degradation by Cu-HNCN/PF system.

and efficient wastewater purification technology.

CRediT authorship contribution statement

Xiao Zhang, Peng Yu, Yongjun Sun: Conceptualization, Methodology, Software, Writing – original draft, Resources, Investigation, Data curation. Xiao Zhang, Baokang Xu, Shiwen Wang, Xi Li, Cheng Wang, Yanhua Xu, Ru Zhou, Yang Yu, Huaili Zheng: Data curation. Xiao Zhang, Baokang Xu, Shiwen Wang, Xi Li, Cheng Wang: Investigation. Yanhua Xu, Yang Yu, Huaili Zheng, Peng Yu, Yongjun Sun: Resources. Xiao Zhang, Yang Yu, Huaili Zheng, Peng Yu, Yongjun Sun: Investigation. Yanhua Xu, Yang Yu, Huaili Zheng, Peng Yu, Yongjun Sun: Supervision. Yanhua Xu, Yang Yu, Huaili Zheng, Peng Yu, Yongjun Sun: Conceptualization, Funding acquisition, Supervision; Xiao Zhang, Peng Yu, Yongjun Sun: Writing – review & editing, Funding acquisition, Supervision.

Declaration of Competing Interest

The authors declare that they have no known competing financial interests or personal relationships that could have appeared to influence the work reported in this paper.

Acknowledgements

Appendix A. Supporting information

Supplementary data associated with this article can be found in the online version at doi:10.1016/j.apcatb.2022.121119.

References

[1] C.-H. Han, H.-D. Park, S.-B. Kim, V. Yargeau, J.-W. Choi, S.-H. Lee, J.-A. Park, Oxidation of tetracycline and oxytetracycline for the photo-Fenton process: their transformation products and toxicity assessment, Water Res. 172 (2020), 115514.

[2] S. Ma, J. Jing, P. Liu, Z. Li, W. Jin, B. Xie, Y. Zhao, High selectivity and effectiveness for removal of tetracycline and its related drug resistance in food wastewater through schwertmannite/graphene oxide catalyzed photo-Fenton-like oxidation, J. Hazard. Mater. 392 (2020), 122437.

[3] S. Xin, B. Ma, G. Liu, X. Ma, C. Zhang, X. Ma, M. Gao, Y. Xin, Enhanced heterogeneous photo-Fenton-like degradation of tetracycline over CuFeO2/biochar catalyst through accelerating electron transfer under visible light, J. Environ. Manag. 285 (2021), 112093.

[4] A.K. Sarmah, M.T. Meyer, A.B.A. Boxall, A global perspective on the use, sales, exposure pathways, occurrence, fate and effects of veterinary antibiotics (VAs) in the environment, Chemosphere 65 (2006) 725–759.

[5] H. Li, C. Shan, B. Pan, Fe (III)-doped g-C3N4 mediated peroxymonosulfate activation for selective degradation of phenolic compounds via high-valent iron-oxo species, Environ. Sci. Technol. 52 (2018) 2197–2205.

[6] Z. Yang, J. Qian, A. Yu, B. Pan, Singlet oxygen mediated iron-based Fenton-like catalysis under nanoconfinement, Proc. Natl. Acad. Sci. USA 116 (2019) 6659–6664.

[7] S. Zhang, T. Hedtke, Q. Zhu, M. Sun, S. Weon, Y. Zhao, E. Stavitski, M. Elimelech, J.-H. Kim, Membrane-confined iron oxychloride nanocatalysts for highly efficient heterogeneous fenton water treatment, Environ. Sci. Technol. (2021).

[8] S. Zhang, M. Sun, T. Hedtke, A. Deshmukh, X. Zhou, S. Weon, M. Elimelech, J.-H. Kim, Mechanism of heterogeneous Fenton reaction kinetics enhancement under nanoscale spatial confinement, Environ. Sci. Technol. 54 (2020) 10868–10875.

[9] X. Zhang, B. Ren, X. Li, B. Liu, S. Wang, P. Yu, Y. Xu, G. Jiang, High-efficiency removal of tetracycline by carbon-bridge-doped g-C3N4/Fe3O4 magnetic heterogeneous catalyst through photo-Fenton process, J. Hazard. Mater. (2021), 126333.

[10] S. Zhang, T. Hedtke, X. Zhou, M. Elimelech, J.-H. Kim, Environmental applications of engineered materials with nanoconfinement, ACS ES T Eng. 1 (2021) 706–724.

[11] Z. Wang, C. Lai, L. Qin, Y. Fu, J. He, D. Huang, B. Li, M. Zhang, S. Liu, L. Li, ZIF-8-modified MnFe2O4 with high crystallinity and superior photo-Fenton catalytic activity by Zn-O-Fe structure for TC degradation, Chem. Eng. J. 392 (2020), 124851.

[12] S. Giannakis, A review of the concepts, recent advances and niche applications of the (photo) Fenton process, beyond water/wastewater treatment: Surface functionalization, biomass treatment, combatting cancer and other medical uses, Appl. Catal. B Environ. 248 (2019) 309–319.

[13] W.-Q. Li, Y.-X. Wang, J.-Q. Chen, N. Hou, Y. Li, X. Liu, R. Ding, G. Zhou, Q. Li, X. Zhou, Boosting photo-Fenton process enabled by ligand-to-cluster charge transfer excitations in iron-based metal organic framework, Appl. Catal. B Environ. (2021), 120882.

[14] M. Liu, H. Xia, W. Yang, X. Liu, J. Xiang, X. Wang, L. Hu, F. Lu, Novel Cu-Fe bi-metal oxide quantum dots coupled g-C3N4 nanosheets with H2O2 adsorption-activation trade-off for efficient photo-Fenton catalysis, Appl. Catal. B Environ. 301 (2022), 120765.

[15] H. Hu, K. Miao, X. Luo, S. Guo, X. Yuan, F. Pei, H. Qian, G. Feng, Efficient Fenton-like treatment of high-concentration chlorophenol wastewater catalysed by Cu-doped SBA-15 mesoporous silica, J. Clean. Prod. 318 (2021), 128632.

[16] J. Xu, X. Zheng, Z. Feng, Z. Lu, Z. Zhang, W. Huang, Y. Li, D. Vuckovic, Y. Li, S. Dai, Organic wastewater treatment by a single-atom catalyst and electrolytically produced H 2 O 2, Nat. Sustain. (2020) 1–9.

[17] G. Pan, Z. Sun, Cu-doped g-C3N4 catalyst with stable Cu0 and Cu+ for enhanced amoxicillin degradation by heterogeneous electro-Fenton process at neutral pH, Chemosphere 283 (2021), 131257.

[18] Y. Tian, N. Jia, H. Ma, G. Liu, Z. Xiao, Y. Wu, L. Zhou, J. Lei, L. Wang, Y. Liu, J. Zhang, 0D/3D coupling of g-C3N4 QDs/hierarchical macro-mesoporous CuO-SiO2 for high-efficiency norfloxacin removal in photo-Fenton-like processes, J. Hazard. Mater. 419 (2021) 126359.

[19] E. Ma, K. Wang, Z. Hu, H. Wang, Dual-stimuli-responsive CuS-based micromotors for efficient photo-Fenton degradation of antibiotics, J. Colloid Interface Sci. 603 (2021) 685–694.

[20] N. Schmachtenberg, S. Silvestri, J. da Silveira Salla, G.L. Dotto, D. Hotza, S.L. Jahn, E.L. Foletto, Preparation of delafossite–type CuFeO2 powders by conventional and microwave–assisted hydrothermal routes for use as photo–Fenton catalysts, J. Environ. Chem. Eng. 7 (2019), 102954.

[21] J. Wang, R. Xu, Y. Li, Y. Li, M. Yang, G. Yang, Y. Zhao, F. Gao, Recent progress, developing strategies, theoretical insights, and perspectives towards high-performance copper single atom electrocatalysts, Mater. Today Energy 21 (2021), 100761.

[22] X. Xie, L. Peng, H. Yang, G.I.N. Waterhouse, L. Shang, T. Zhang, MIL-101–derived mesoporous carbon supporting highly exposed Fe single-atom sites as efficient oxygen reduction reaction catalysts, Adv. Mater. 33 (2021), 2101038.

[23] Y. Long, J. Dai, S. Zhao, Y. Su, Z. Wang, Z. Zhang, Atomically dispersed cobalt sites on graphene as efficient periodate activators for selective organic pollutant degradation, Environ. Sci. Technol. 55 (2021) 5357–5370.

[24] W. Wang, Z. Zeng, G. Zeng, C. Zhang, R. Xiao, C. Zhou, W. Xiong, Y. Yang, L. Lei, Y. Liu, D. Huang, M. Cheng, Y. Yang, Y. Fu, H. Luo, Y. Zhou, Sulfur doped carbon quantum dots loaded hollow tubular g-C3N4 as novel photocatalyst for destruction of Escherichia coli and tetracycline degradation under visible light, Chem. Eng. J. 378 (2019), 122132.

[25] X. Zhang, B. Ren, X. Li, Y. Xu, B. Liu, P. Yu, Y. Sun, D. Mei, Efficiently enhanced visible-light photocatalytic activity by in situ deposition of Ag@ AgBr on g-C3N4/Fe3O4 magnetic heterogeneous materials, Sep. Purif. Technol. 254 (2021), 117596.

[26] S. An, G. Zhang, T. Wang, W. Zhang, K. Li, C. Song, J.T. Miller, S. Miao, J. Wang, X. Guo, High-density ultra-small clusters and single-atom Fe sites embedded in graphitic carbon nitride (g-C3N4) for highly efficient catalytic advanced oxidation processes, ACS Nano 12 (2018) 9441–9450.

[27] X. Zhang, B. Xu, S. Wang, X. Li, C. Wang, B. Liu, F. Han, Y. Xu, P. Yu, Y. Sun, Tetracycline degradation by peroxymonosulfate activated with CoNx active sites: performance and activation mechanism, Chem. Eng. J. (2021), 133477.

[28] J. Xu, X. Zheng, Z. Feng, Z. Lu, Z. Zhang, W. Huang, Y. Li, D. Vuckovic, Y. Li, S. Dai, Organic wastewater treatment by a single-atom catalyst and electrolytically produced H 2 O 2, Nat. Sustain. 4 (2021) 233–241.

[29] X. Zhang, B. Xu, S. Wang, X. Li, B. Liu, Y. Xu, P. Yu, Y. Sun, High-density dispersion of CuNx sites for H2O2 activation toward enhanced Photo-Fenton performance in antibiotic contaminant degradation, J. Hazard. Mater. (2021), 127039.

[30] C.-C. Wang, X.-H. Yi, P. Wang, Powerful combination of MOFs and C3N4 for enhanced photocatalytic performance, Appl. Catal. B Environ. 247 (2019) 24–48.

[31] X.-H. Li, J. Zhang, X. Chen, A. Fischer, A. Thomas, M. Antonietti, X. Wang, Condensed graphitic carbon nitride nanorods by nanoconfinement: promotion of crystallinity on photocatalytic conversion, Chem. Mater. 23 (2011) 4344–4348.

[32] X. Wang, K. Shinokita, H.E. Lim, N.B. Mohamed, Y. Miyauchi, N.T. Cuong, S. Okada, K. Matsuda, Direct and indirect exciton dynamics in few-layered ReS2 revealed by photoluminescence and pump-probe spectroscopy, Adv. Funct. Mater. 29 (2019), 1806169.

[33] X. Qiu, Y. Zhang, Y. Zhu, C. Long, L. Su, S. Liu, Z. Tang, Applications of nanomaterials in asymmetric photocatalysis: recent progress, challenges, and opportunities, Adv. Mater. 33 (2021), 2001731.

[34] X. Wang, J.I. Feng, Y. Bai, Q. Zhang, Y. Yin, Synthesis, properties, and applications of hollow micro-/nanostructures, Chem. Rev. 116 (2016) 10983–11060.

[35] Z. Mo, H. Xu, Z. Chen, X. She, Y. Song, J. Wu, P. Yan, L. Xu, Y. Lei, S. Yuan, H. Li, Self-assembled synthesis of defect-engineered graphitic carbon nitride nanotubes for efficient conversion of solar energy, Appl. Catal. B Environ. 225 (2018) 154–161.

[36] M. Wu, Q. Li, C. Chen, G. Su, M. Song, B. Sun, J. Meng, B. Shi, Constructed palladium-anchored hollow-rod-like graphitic carbon nitride created rapid visible-light-driven debromination of hexabromocyclododecane, Appl. Catal. B Environ. 297 (2021), 120409.

[37] Z. Tong, D. Yang, Y. Sun, Y. Nan, Z. Jiang, Tubular g-C3N4 isotype heterojunction: enhanced visible-light photocatalytic activity through cooperative manipulation of oriented electron and hole transfer, Small 12 (2016) 4093–4101.

[38] Q. Gao, S. Hu, Y. Du, Z. Hu, The origin of the enhanced photocatalytic activity of carbon nitride nanotubes: a first-principles study, J. Mater. Chem. A 5 (2017) 4827–4834.

[39] J. Fu, B. Zhu, C. Jiang, B. Cheng, W. You, J. Yu, Hierarchical porous O-doped g-C3N4 with enhanced photocatalytic CO2 reduction activity, Small 13 (2017), 1603938.

[40] L. Yu, H. Hu, H.B. Wu, X.W. Lou, Complex hollow nanostructures: synthesis and energy-related applications, Adv. Mater. 29 (2017), 1604563.

[41] A. Serrà, E. Gómez, J. Michler, L. Philippe, Facile cost-effective fabrication of Cu@ Cu2O@CuO–microalgae photocatalyst with enhanced visible light degradation of tetracycline, Chem. Eng. J. 413 (2021), 127477.

[42] J. Sun, S. Yang, Z. Liang, X. Liu, P. Qiu, H. Cui, J. Tian, Two-dimensional/one-dimensional molybdenum sulfide (MoS2) nanoflake/graphitic carbon nitride (g-C3N4) hollow nanotube photocatalyst for enhanced photocatalytic hydrogen production activity, J. Colloid Interface Sci. 567 (2020) 300–307.

[43] W.-J. Jiang, L. Gu, L. Li, Y. Zhang, X. Zhang, L.-J. Zhang, J.-Q. Wang, J.-S. Hu, Z. Wei, L.-J. Wan, Understanding the high activity of Fe–N–C electrocatalysts in oxygen reduction: Fe/Fe3C nanoparticles boost the activity of Fe–N x, J. Am. Chem. Soc. 138 (2016) 3570–3578.

[44] X. Zhang, B. Ren, Y. Xu, X. Li, P. Yu, Y. Sun, H. Zheng, Catalytic oxidation of toluene in air using manganese incorporated catalyst by non-thermal plasma system, Sep. Purif. Technol. 257 (2021), 117973.

[45] Z. Huang, P. Wu, C. Liu, M. Chen, S. Yang, Z. Dang, N. Zhu, Multiple catalytic reaction sites induced non-radical/radical pathway with graphene layers

encapsulated Fe-N-C toward highly efficient peroxymonosulfate (PMS) activation, Chem. Eng. J. 413 (2021), 127507.

[46] S. Guo, Z. Deng, M. Li, B. Jiang, C. Tian, Q. Pan, H. Fu, Phosphorus-doped carbon nitride tubes with a layered micro-nanostructure for enhanced visible-light photocatalytic hydrogen evolution, Angew. Chem. 128 (2016) 1862–1866.

[47] P. Niu, L. Zhang, G. Liu, H.M. Cheng, Graphene-like carbon nitride nanosheets for improved photocatalytic activities, Adv. Funct. Mater. 22 (2012) 4763–4770.

[48] J. Zhang, M. Zhang, C. Yang, X.J.A.M. Wang, Nanospherical carbonnitride frameworks with sharp edges accelerating charge collection andseparation at a soft photocatalytic interface, Adv. Mater. 26 (2014) 4121–4126.

[49] W. Liu, Y. Li, F. Liu, W. Jiang, D. Zhang, J. Liang, Visible-light-driven photocatalytic degradation of diclofenac by carbon quantum dots modified porous g-C3N4: mechanisms, degradation pathway and DFT calculation, Water Res. 151 (2019) 8–19.

[50] M. Wu, X. He, B. Jing, T. Wang, C. Wang, Y. Qin, Z. Ao, S. Wang, T. An, Novel carbon and defects co-modified g-C3N4 for highly efficient photocatalytic degradation of bisphenol A under visible light, J. Hazard. Mater. 384 (2020), 121323.

[51] Z. Huang, H. Chen, X. He, W. Fang, X. Du, W. Li, X. Zeng, L. Zhao, A bibendum-like structure of carbon nitride microtubes with regular arrangement nanotubes for photocatalytic protons reduction, Mater. Today Energy (2021), 100767.

[52] W. Fan, Z. Li, C. You, X. Zong, X. Tian, S. Miao, T. Shu, C. Li, S. Liao, Binary Fe, Cu-doped bamboo-like carbon nanotubes as efficient catalyst for the oxygen reduction reaction, Nano Energy 37 (2017) 187–194.

[53] S. Sarkar, S.S. Sumukh, K. Roy, N. Kamboj, T. Purkait, M. Das, R.S. Dey, Facile one step synthesis of Cu-g-C3N4 electrocatalyst realized oxygen reduction reaction with excellent methanol crossover impact and durability, J. Colloid Interface Sci. 558 (2020) 182–189.

[54] Y. Lu, C.L. Dong, Y.C. Huang, Y. Zou, Z. Liu, Y. Liu, Y. Li, N. He, J. Shi, S. Wang, Identifying the geometric site dependence of spinel oxides for the electrooxidation of 5–hydroxymethylfurfural, Angew. Chem. 132 (2020) 19377–19383.

[55] X. Wang, K. Maeda, X. Chen, K. Takanabe, K. Domen, Y. Hou, X. Fu, M. Antonietti, Polymer semiconductors for artificial photosynthesis: hydrogen evolution by mesoporous graphitic carbon nitride with visible light, J. Am. Chem. Soc. 131 (2009) 1680–1681.

[56] M. Kawase, K. Akaike, K. Aoyama, Y. Ito, M. Tamura, K. Kanai, Elucidation of the enhanced photoactivity of melon calcined with MoO3, Appl. Catal. B Environ. 273 (2020) 119068.

[57] Y. Yan, X. Zhou, P. Yu, Z. Li, T. Zheng, Characteristics, mechanisms and bacteria behavior of photocatalysis with a solid Z-scheme Ag/AgBr/g-C3N4 nanosheet in water disinfection, Appl. Catal. A Gen. 590 (2020), 117282.

[58] J. Jiang, X. Wang, Y. Liu, Y. Ma, T. Li, Y. Lin, T. Xie, S. Dong, Photo-Fenton degradation of emerging pollutants over Fe-POM nanoparticle/porous and ultrathin g-C3N4 nanosheet with rich nitrogen defect: Degradation mechanism, pathways, and products toxicity assessment, Appl. Catal. B Environ. 278 (2020), 119349.

[59] J. Liang, W. Zhang, Z. Zhao, W. Liu, J. Ye, M. Tong, Y. Li, Different degradation mechanisms of carbamazepine and diclofenac by single-atom Barium embedded g-C3N4: the role of photosensitation-like mechanism, J. Hazard. Mater. 416 (2021), 125936.

[60] C. Liu, S. Dong, Y. Chen, Enhancement of visible-light-driven photocatalytic activity of carbon plane/g-C3N4/TiO2 nanocomposite by improving heterojunction contact, Chem. Eng. J. 371 (2019) 706–718.

[61] J. Hu, P. Zhang, W. An, L. Liu, Y. Liang, W. Cui, In-situ Fe-doped g-C3N4 heterogeneous catalyst via photocatalysis-Fenton reaction with enriched photocatalytic performance for removal of complex wastewater, Appl. Catal. B Environ. 245 (2019) 130–142.

[62] X. Zhang, X. Xie, H. Wang, J. Zhang, B. Pan, Y. Xie, Enhanced photoresponsive ultrathin graphitic-phase C3N4 nanosheets for bioimaging, J. Am. Chem. Soc. 135 (2013) 18–21.

[63] H. Fang, H.A. Bechtel, E. Plis, M.C. Martin, S. Krishna, E. Yablonovitch, A. Javey, Quantum of optical absorption in two-dimensional semiconductors, Proc. Natl. Acad. Sci. USA 110 (2013) 11688–11691.

[64] M. Moztahida, M. Nawaz, J. Kim, A. Shahzad, S. Kim, J. Jang, D.S. Lee, Reduced graphene oxide-loaded-magnetite: a Fenton-like heterogeneous catalyst for

[65] photocatalytic degradation of 2-methylisoborneol, Chem. Eng. J. 370 (2019) 855–865.

[65] F. Li, M. Tang, T. Li, L. Zhang, C. Hu, Two-dimensional graphene/g-C3N4 in-plane hybrid heterostructure for enhanced photocatalytic activity with surface-adsorbed pollutants assistant, Appl. Catal. B Environ. 268 (2020), 118397.

[66] Y. Li, M. Gu, T. Shi, W. Cui, X. Zhang, F. Dong, J. Cheng, J. Fan, K. Lv, Carbon vacancy in C3N4 nanotube: electronic structure, photocatalysis mechanism and highly enhanced activity, Appl. Catal. B Environ. 262 (2020), 118281.

[67] Y. Yao, G. Wu, F. Lu, S. Wang, Y. Hu, J. Zhang, W. Huang, F. Wei, Enhanced photo-Fenton-like process over Z-scheme CoFe2O4/gC3N4 heterostructures under natural indoor light, Environ. Sci. Pollut. Res. 23 (2016) 21833–21845.

[68] Y. Liu, X. He, Y. Fu, D.D. Dionysiou, Degradation kinetics and mechanism of oxytetracycline by hydroxyl radical-based advanced oxidation processes, Chem. Eng. J. 284 (2016) 1317–1327.

[69] H. Qi, X. Sun, Z. Sun, Porous graphite felt electrode with catalytic defects for enhanced degradation of pollutants by electro-Fenton process, Chem. Eng. J. 403 (2021), 126270.

[70] C. Lai, F. Huang, G. Zeng, D. Huang, L. Qin, M. Cheng, C. Zhang, B. Li, H. Yi, S. Liu, L. Li, L. Chen, Fabrication of novel magnetic MnFe2O4/bio-char composite and heterogeneous photo-Fenton degradation of tetracycline in near neutral pH, Chemosphere 224 (2019) 910–921.

[71] L. Tang, C. Feng, Y. Deng, G. Zeng, J. Wang, Y. Liu, H. Feng, J. Wang, Enhanced photocatalytic activity of ternary Ag/g-C3N4/NaTaO3 photocatalysts under wide spectrum light radiation: the high potential band protection mechanism, Appl. Catal. B Environ. 230 (2018) 102–114.

[72] M. Zhang, X. Chen, H. Zhou, M. Murugananthan, Y. Zhang, Degradation of p-nitrophenol by heat and metal ions co-activated persulfate, Chem. Eng. J. 264 (2015) 39–47.

[73] S. Liu, C. Lai, B. Li, C. Zhang, M. Zhang, D. Huang, L. Qin, H. Yi, X. Liu, F. Huang, X. Zhou, L. Chen, Role of radical and non-radical pathway in activating persulfate for degradation of p-nitrophenol by sulfur-doped ordered mesoporous carbon, Chem. Eng. J. 384 (2020), 123304.

[74] Y. Yin, R. Jia, W. Zhang, Y. Ren, X. Li, M. Hua, L. Lv, Electron-rich oxygen enhanced Fe-doped g-C3N4 mediated Fenton-like process: accelerate Fe(III) reduction and strengthen catalyst stability, J. Clean. Prod. 319 (2021), 128680.

[75] F.-X. Wang, C.-C. Wang, X. Du, Y. Li, F. Wang, P. Wang, Efficient removal of emerging organic contaminants via photo-Fenton process over micron-sized Fe-MOF sheet, Chem. Eng. J. 429 (2022), 132495.

[76] B. Li, W. Song, H. Wu, Z. Liu, Y. Teng, Y. Sun, Y. Xu, H. Zheng, Degradation of norfloxacin with peroxymonosulfate activated by nanoconfinement Co3O4@CNT nanocomposite, Chem. Eng. J. 398 (2020), 125498.

[77] Y. Yin, R. Lv, X. Li, L. Lv, W. Zhang, Exploring the mechanism of ZrO2 structure features on H2O2 activation in Zr–Fe bimetallic catalyst, Appl. Catal. B Environ. 299 (2021), 120685.

[78] B. Liu, S. Pan, Z. Liu, X. Li, X. Zhang, Y. Xu, Y. Sun, Y. Yu, H. Zheng, Efficient removal of Cu(II) organic complexes by polymer-supported, nanosized, and hydrated Fe(III) oxides through a Fenton-like process, J. Hazard. Mater. 386 (2020), 121969.

[79] B. Liu, W. Song, H. Wu, Y. Xu, Y. Sun, Y. Yu, H. Zheng, S. Wan, Enhanced oxidative degradation of norfloxacin using peroxymonosulfate activated by oily sludge carbon-based nanoparticles CoFe2O4/OSC, Chem. Eng. J. 400 (2020), 125947.

[80] H. Wang, Y. Wu, M. Feng, W. Tu, T. Xiao, T. Xiong, H. Ang, X. Yuan, J.W. Chew, Visible-light-driven removal of tetracycline antibiotics and reclamation of hydrogen energy from natural water matrices and wastewater by polymeric carbon nitride foam, Water Res. 144 (2018) 215–225.

[81] X. Zhang, Z. Yao, Y. Zhou, Z. Zhang, G. Lu, Z. Jiang, Theoretical guidance for the construction of electron-rich reaction microcenters on C–O–Fe bridges for enhanced Fenton-like degradation of tetracycline hydrochloride, Chem. Eng. J. 411 (2021), 128535.

[82] I.A. Vasiliadou, R. Molina, F. Martinez, J.A. Melero, P.M. Stathopoulou, G. Tsiamis, Toxicity assessment of pharmaceutical compounds on mixed culture from activated sludge using respirometric technique: the role of microbial community structure, Sci. Total Environ. 630 (2018) 809–819.